Exclusive η Meson Reconstruction in Proton-Proton Collisions at 2.2 GeV with the HADES Spectrometer and High Resolution Tracking

Vom Fachbereich Physik
der Technischen Universität Darmstadt

zur Erlangung des Grades
eines Doktors der Naturwissenschaften
(Dr. rer. nat.)

genehmigte Dissertation von

Master-Phys. Anar Rustamov
aus Shamakhi, Aserbaidschan

Referent: Prof. Dr. Peter Braun-Munzinger
Korreferent: Prof. Dr. Jochen Wambach

Tag der Einreichung: 5. Juli 2006
Tag der Prüfung: 26. Juli 2006

Darmstadt 2006
D17

Declaration of Originality

With this I confirm that this doctoral thesis contains the results of my research carried out at GSI in Darmstadt.

Excluding an introductory part the research described in this thesis is original unless an explicit reference is made to work of others. I further state that no part of this thesis has been submitted for any qualification other than the degree Dr. rer. nat. at the Technical University of Darmstadt.

Zusammenfassung

HADES (**H**igh **A**cceptance **D**i**E**lectron **S**pectrometer) ist ein Di-Elektronen-Spektrometer, das am Schwer Ionen Synchrotron (SIS) an der GSI in Darmstadt aufgebaut wurde.

Das Physik Programm von HADES befasst sich hauptsächlich mit den in-Medium Eigenschaften der leichten Vektormesonen $\rho(770)$, $\omega(783)$ und $\phi(1020)$, sowie verschiedenen anderen wichtigen Fragestellungen der Physik der Hadronen, wie etwa der Gültigkeit des Vektordominanzmodells (VDM) zur Beschreibung von Meson und Baryon-Dalitzzerfällen und dem elektromagnetischen Formfaktor des Nukleons in der zeitartigen Region.

Die vorliegende Arbeit präsentiert eine detaillierte Analyse der exklusiven Rekonstuktion des η-Mesons in Proton-Proton- Kollisionen bei einer kinetischen Energie des einfallenden Protons von 2,2 GeV. Die exklusive Messung des η-Mesons wurde in den zwei elektromagnetischen Zerfallskanälen des η-Mesons ($\eta \to \pi^+\pi^-\pi^0$ und $\eta \to e^+e^-\gamma$), deren relatives Verzweigungsverhältnis bekannt ist, durchgeführt.

Um die Impulsauflösung der Spurrekonstruktion und damit die Auflösung des Experimentes in der invarianten Masse zu verbessern, wurde ein Algorithmus zur simultanen Anpassung der rekonstruierten Teilchenspuren unter Ausnutzung der kinematischen Randbedingungen entwickelt. Die Ergebnisse dieser Untersuchung wurden zur Bestimmung der Rekonstruktionseffizienz des HADES-Experimentes für Di-Elektronen verwendet.

Anhand der kinematischen Daten der elastischen Proton-Proton Streuung wurde die Auflösung der Spurrekonstruktion und die Ausrichtung der Detektoren im Raum untersucht.

Desweiteren wurde eine Methode zur Impulsrekonstruktion der Teilchenspuren entwickelt, die auf der Verwendung eines kubischen Splines als Spurmodell im Bereich des magnetischen Feldes basiert. Die in den Driftkammern des Spektrometers rekonstruierten Teilchenspuren wurden durch eine weitere, im Rahmen dieser Arbeit entwickelte, Methode mit den Spurpunkten der Spuren in den Flugzeitwänden korreliert. Beide Methoden wurden für die Analyse in der vorliegenden Arbeit verwendet.

Aufgrund der unterschiedlichen Phasenraumverteilung der obengenannten Zerfallskanäle ist die Akzeptanz des HADES-Spektrometers fuer die Zerfallsprodukte aus beiden Kanälen ebenfalls verschieden. Daher wurde durch eine Simulation das relative Verzweigungsverhältnis innerhalb der Akzeptanz des HADES-Spektrometers bestimmt. Es wurden verschiedene anisotrope Winkelverteilung des η-Mesons, wie sie vom DISTO-Experiment beobachtet wurden, simuliert und mit den gemessenen Daten verglichen.

Im Vektordominanzmodell wechselwirkt das Photon mit einem Hadron nicht nur direkt, sondern auch durch Vektormesonen. Insbesondere für das neutrale pseudoskalare η-Meson erfolgt der Dalitz-Zerfall in zwei Schritten: Zuerst werden zwei Photonen (reell und virtuell) emittiert, danach zerfällt das virtuelle Photon in ein e^+e^- Paar.

Die Gültigkeit der Beschreibung des Dalitz-Zerfalls des η- Mesons durch das VDM wurde durch einen Vergleich mit der experimentell rekonstruierten invarianten Massenverteilung der e^+e^- Paare geprüft.

Der Produktionsmechnismus des η-Mesons wurde anhand der Winkelverteilung der Mesonen im Schwerpunktsystem untersucht.

Die vorliegende Arbeit unterteilt sich in zwei Teile:

Der erste Teil gibt eine kurze Beschreibung des Physik Programs des HADES-Experimentes, eine Beschreibung des Spektrometers und eine detaillierte Darstellung der Spurrekonstruktionsalgorithmen.

Der zweite Teil der Arbeit befasst sich mit der Analyse der Proton-Proton-Daten und den obengenannten Untersuchungen, sowie der Diskussion der Resultate.

Abstract

HADES (**H**igh **A**cceptance **D**i**E**lectron **S**pectrometer) is a unique apparatus currently assembled at heavy-ion synchrotron SIS at GSI, Darmstadt.

The main part of the HADES physics program is focused on in-medium properties of the light vector mesons $\rho(770)$, $\omega(783)$ and $\phi(1020)$, but also concerns several important problems of hadron physics like: validity of the **V**ector meson **D**ominance **M**odel (VDM) in the description of meson and baryon Dalitz decays and of the electromagnetic form-factor of the nucleon in time-like region.

In the framework of the present thesis a detailed study of the exclusive η meson reconstruction in proton-proton collisions at 2.2 GeV kinetic energy of the incident proton beam is presented. The exclusive measurement of the η mesons has been performed for two electromagnetic decay channels ($\eta \to \pi^+\pi^-\pi^0$ and $\eta \to e^+e^-\gamma$), the relative branching ratios of which are known.

In order to obtain better tracking resolution, an algorithm of kinematic fit has been developed and tested. The main goal of the kinematic fit is to improve the reconstruction resolution by using physical constraints governing the process. Studied results have been used to evaluate the dielectron detection efficiency of the HADES experiment. The kinematic fit algorithm has been used for above mentioned analysis as well.

Apart from these studies, using the kinematics of the elastic scattering channel, the spectrometer performance has been studied in terms of reconstruction resolution and detector alignments.

From a technical point of view, a new method for momentum reconstruction, using a cubic spline track model in the magnetic field region of the HADES spectrometer, has been developed. An algorithm for matching of different hits belonging to one track reconstructed by the spectrometer systems has also been developed. Both algorithms have been used for the data analysis described in this work.

The phase-space distributions of $\eta \to \pi^+\pi^-\pi^0$ and $\eta \to e^+e^-\gamma$ decay channels being different, the relative branching ratio of these decay channels will differ from that obtained for full phase space. Therefore the simulation data has been generated in order to find out the relative branching ratios of the above mentioned decay channels inside the HADES acceptance. We have done different types of simulations in order to compare with the data. In particular, the anisotropy in the angular distributions of the η mesons, observed by the DISTO experiment, have been included in the simulation and compared with our data.

According to the VDM, the photon interacts with the hadron of interest not only directly, but also through vector mesons. In particular for the η meson, which is a neutral pseudoscalar meson, the Dalitz decay goes in two steps, where in a first step it emits two photons (real plus virtual), and in a second step the virtual photon decays into a e^+e^- pair.

The validity of the VDM model in describing the Dalitz decay of the η meson has been investigated by comparing the experimentally reconstructed invariant-mass distribution of the e^+e^- pairs with the VDM model predictions.

To investigate the production mechanism of the η meson, their angular distributions in the center-of-mass system have been studied.

This thesis is divided into two parts:

In the first part a brief introduction to the physics program of the HADES experiment is given. A description of the detector systems of the spectrometer and the detailed explanation of track reconstruction algorithm of the HADES experiment is given in this part as well.

The second part mainly concerns the analysis of the proton-proton data and the discussion of the results.

Contents

List of Figures

List of Tables

Part I

Physics motivation, spectrometer setup and tracking

Chapter 1

Physics motivation

1.1 Vector meson Dominance Model

One of the physics goals of the HADES experiment is to test the validity of the Vector meson Dominance Model in describing the Dalitz decays of mesons.

The vector mesons ρ,ω,ϕ play a special role in the description of hadronic interactions in the non-perturbative QCD regime. In this regime, effective hadron models use composite hadrons and mesons as field carriers instead of quarks and gluons.

The discrepancy of magnetic moments of protons and neutrons from their Dirac values ($1\mu_b$ and 0 correspondingly) was explained as a possibility for the nucleon to be a composite system of an idealized (bare) nucleon and a π meson cloud. In this schema, a proton is existing part of the time as a bare one with a π^0 cloud and another part as a bare neutron with a π^+ cloud. Qualitative estimation of the π meson cloud radius gives as a result a value of the order of the Compton wave length for pions. Thus the above schema predicts that the electric charge inside a proton is not concentrated at a point but spread in a finite volume.

Taking into account this interpretation, the interaction of fast electrons with a nucleon can be explained with Feynman diagrams as shown in Figure 1.1. The left part of the Figure expresses the net effect consisting of several parts on the right side [1]:

- One photon
- Two virtual pions from the pion cloud
- Three virtual pions from the pion cloud
- etc.

Theoretical calculations have shown that this picture explains the experimentally obtained data on form factors if one assumes a strong resonant interaction between pions

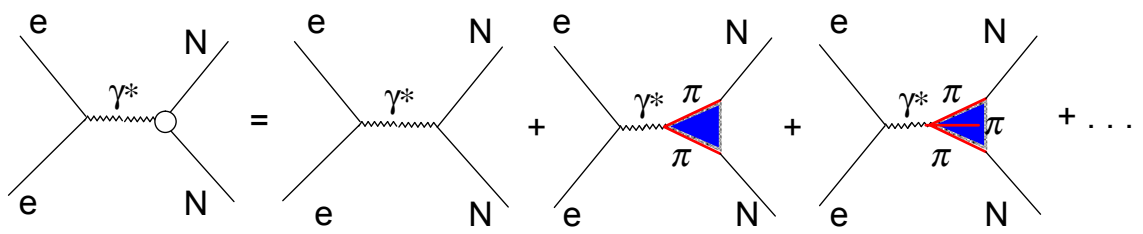

Figure 1.1: Interaction of fast electrons with hadrons through one photon, two virtual pions, three virtual pions and so on [1].

and assumes the systems of two and three pions as new particles: vector mesons [1, 3, 4] (Shaded area in Figure 1.1).

It turns out, that in contrast to the case of space-like momentum transfers where the form factors of charged particles decrease as q^2 increases, another spectacular phenomenon arises in the case of time-like momentum transfers. A virtual photon can interact with a hadron of interest not only directly, but also after a transition to a virtual vector meson state [2]. This is the essential idea behind the **V**ector meson **D**ominance **M**odel (VDM).

In the field theory, the particle interactions are described via Lagrangian (L), which depends on field (φ) and its first derivative ($\partial_\mu\varphi$), of interacting currents and fields. There one obtains the equations of motion by requiring the variation of the action $S = \int d^4xL$ to vanish:

$$\frac{\delta S}{\delta \varphi} = 0 \tag{1.1}$$

which leads to the so called Euler-Lagrange equations:

$$\frac{\partial L}{\partial \varphi} - \partial_\mu \frac{\partial L}{\partial(\partial_\mu \varphi)} = 0 \tag{1.2}$$

For example, the Lagrangian for free fermion with mass m can be written as:

$$L = \bar{\psi}(i\gamma^\mu \partial_\mu - m)\psi \tag{1.3}$$

This Lagrangian is not invariant under local gauge transformations:

$$\psi \rightarrow \psi' = e^{iQ\theta(x)}\psi \tag{1.4}$$

because $\partial_\mu\psi$ which enters into 1.3 will transform as:

$$\partial_\mu\psi \rightarrow e^{iQ\theta(x)}\left(\partial_\mu + iQ\partial_\mu\theta(x)\right)\psi \tag{1.5}$$

where the term $iQ\partial_\mu\theta(x)\psi$ breaks the symmetry. But we want the Lagrangian to be invariant under the local transformations as well. This can be done by introducing a covariant derivative D_μ which transforms as the field does:

$$D_\mu\psi \rightarrow (D_\mu\psi)' = e^{iQ\theta(x)}D_\mu\psi \tag{1.6}$$

If we manage to build such a covariant derivative the Lagrangian 1.3 will be invariant under the local transformations as well.

Our aim was to eliminate the symmetry breaking term which has a Lorentz index, therefore the covariant derivative should also contain something with Lorentz index, which we will denote as A_μ

$$D_\mu\psi \equiv (\partial_\mu - ieQA_\mu)\psi \tag{1.7}$$

where e is called a coupling constant.

In order for the covariant derivative to transform like 1.6, the introduced field should transform like:

$$A_\mu \rightarrow A_\mu + \frac{1}{e}\partial_\mu\theta(x) \tag{1.8}$$

Now we can write a Lagrangian 1.3 with the covariant derivative

$$L = \bar{\psi}(i\gamma^\mu D_\mu - m)\psi \tag{1.9}$$

which is clearly invariant under local transformations.

Substituting definition of of the covariant derivative from 1.7 into Lagrangian 1.9 we have

$$L = \bar{\psi}(i\gamma^\mu\partial_\mu - m)\psi + eQA_\mu(\bar{\psi}\gamma^\mu\psi) \tag{1.10}$$

By comparing this Lagrangian with the Lagrangian for interacting electron and photon fields one can easily see that the introduced fields A_μ are nothing but the photon field.

We can write the interaction term in the Lagrangian as:

$$L^{em}_{int} = ej^{em}_\mu A^\mu \tag{1.11}$$

Summarizing, by requiring the local gauge invariance of the Lagrangian for free fermion field we had to introduce a photon field and got the interaction term in the Lagrangian, which describes the interaction of fermions with photon. One can also note that it is automatically obtained that photon should be massless because the Lagrangian 1.10 does not contain a mass term for the photon.

In a similar way in order to preserve the invariance of the free Lagrangian under local SU(2) isotopic transformations:

$$\psi \rightarrow e^{i\frac{\tau_\alpha}{2}\theta_\alpha(x)} \tag{1.12}$$

where τ_α are Pauli matrices, one has to introduce the vector meson fields.
The corresponding interaction term can be written as [1]:

$$g\rho^\alpha_\mu \bar{\psi}\gamma^\mu(\tau_\alpha/2)\psi \tag{1.13}$$

where g is the corresponding coupling constant and ρ_μ is the vector meson field.
Similar to 1.11 we can write an interaction term in Lagrangian as:

$$L^h_{int} = g j^\alpha_\mu \rho^\mu_\alpha \tag{1.14}$$

where $\vec{j_\mu}$ is the hadronic vector current and $\vec{\rho^\mu}$ is the vector meson field.

In other words the requirement of the invariance of the free Lagrangian under local isotopic rotations gives an interactions term in the Lagrangian with vector mesons. As the vector mesons and a photon has the same quantum numbers a virtual photon can interact with a hadron after a transition to a virtual vector meson state.

The coupling constants (g_v) of the vector mesons into photons can be obtained from the measured dielectron decay widths of the vector mesons. For any vector meson V with a mass m_v, neglecting the electron mass, the decay width into e^+e^- pairs can be written as [3]:

$$\Gamma(V \rightarrow e^+e^-) = \frac{4\pi\alpha^2}{3g_v^2} m_v \tag{1.15}$$

According to Equation 1.15 the ratios of $\Gamma_V^{e^+e^-}$ for the ρ, ω and ϕ mesons are proportional to m_v/g_v^2. The coupling constants g_v can be expressed with a help of one universal coupling constant g_γ:

$$\Gamma_\rho^{e^+e^-} : \Gamma_\omega^{e^+e^-} : \Gamma_\phi^{e^+e^-} = \frac{m_\rho}{g_\gamma^2} : \frac{m_\omega}{9g_{\gamma^2}} : \frac{m_\phi}{4.5g_\gamma^2} \approx 1 : 9 : 4.5 \tag{1.16}$$

for $g_\gamma = 5.7 \approx g_\rho$.

VDM hypothesis also assumes that the same coupling $g = g_\gamma$ describes also the meson-hadron interactions (See Equation 1.14). This can be verified by an analysis of the di-pion decay width of ρ meson. The corresponding width is given by [5]

$$\Gamma(\rho \rightarrow \pi^+\pi^-) = \frac{2}{3}\frac{|p_{cm}|^3}{m_\rho^2}\frac{f^4_{\rho\pi\pi}}{4\pi} \tag{1.17}$$

[1] Here we show an example for the case when the ψ field is an iso-doublet. In general the covariant derivative introduced in this case has a form $\partial_\mu\psi \rightarrow \partial_\mu\psi - ig\vec{\rho}_\mu\vec{T}\psi$. In our example when ψ field is an iso-doublet the matrix $\vec{T}$ is $\vec{\tau}/2$.

where $|p_{cm}| = \sqrt{(m_\rho/2)^2 - m_\pi^2}$

Taking the experimental value of $\Gamma(\rho \to \pi^+\pi^-)$ one can obtain $f_\rho\pi\pi = 6.05$ which is close to the universal coupling constant $g_\gamma = 5.7$.

1.2 Dalitz decays of mesons and transition form factors

The process of single-photon exchange described in the previous section is forbidden for neutral mesons A (e.g., π^0,η,η'). Indeed, the neutral particle being identical to its antiparticle, it transforms into itself under charge conjugation. Consequently, the wave function of a neutral particle either remains unaffected by charge conjugation or only reverses its sign. Electromagnetic forces are responsible for the decay of π^0, η and η' mesons into two γ quanta. Therefore the charge conjugation parity of such neutral particles is a positive quantity. As the photon, being the quantum of the electromagnetic field, has a negative charge-conjugation parity the one photon exchange breaks the conservation of the charge conjugation parity.

However, a neutral particle with a given charge-conjugation parity can convert as a result of the interaction into another particle with the sign-reversed value of this quantum number. Therefore decays of the type $A \to Be^+e^-$ are not real multi body decays (for which usually the name Dalitz is used) but can be reduced to a decay into B plus a virtual photon (with an invariant mass $m^2_{e^+e^-}$) and subsequent conversion of the latter [6].

The probability of formation of a lepton pair with an effective mass $m_{l^+l^-}$ in a conversion decay, $A \to B + l^+ + l^-$, is proportional to the probability of emitting a virtual γ quantum with time-like 4-momentum $q^2 = m^2_{l^+l^-}$. However, the probability of emission of this photon is determined by the dynamic structure arising at the vertex of the transition. This structure which is due to the cloud of virtual states in the region of the transition $A \to B$ is characterized by a transition form factor.

The transition form factor can be obtained by studying the probability of the decay $A \to B + l^+ + l^-$ as a function of the squared effective mass of the lepton pair, $q^2 = m^2_{l^+l^-}$. Referred to a unit interval of q^2, this probability gives so-called spectrum of effective mass of lepton pairs, $d\Gamma/dq^2$.

If the particles A and B were structureless objects, it would be possible to calculate the mass spectrum of leptonic pairs, $[d\Gamma/dq^2]_{pointlike}$ with high accuracy, by the methods of quantum electrodynamics. The complicated internal structure of particles modifies this spectrum:

$$d\Gamma/dq^2 = [d\Gamma/dq^2]_{pointlike}|F_{AB}(q^2)|^2 \tag{1.18}$$

By comparing the measured spectrum of lepton pairs with pure QED calculations for point-like particles, it is possible to determine experimentally the transition form factor $|F_{AB}(q^2)|^2$ in the time-like region of momentum transfer.

The decays $P \rightarrow \gamma + l^+ + l^-$ occupy a special place. In this case the transition form factor describes the electromagnetic structure of the vertex $P \rightarrow \gamma$ which incorporates only one hadron, the decaying meson.

The leptonic pair mass spectrum of the decays of type:

$$P \rightarrow e^+e^-\gamma \tag{1.19}$$

normalized to the total probability of radiative transition is defined as [2]:

$$\frac{d\Gamma(P \rightarrow e^+e^-\gamma)}{dq^2\Gamma(P \rightarrow \gamma\gamma)} = \frac{2\alpha}{3\pi}\left[1 - \frac{4m_e^2}{q^2}\right]^{1/2}\left[1 + 2\frac{m_e^2}{q^2}\right]\frac{1}{q^2}\left[1 - \frac{q^2}{m_p^2}\right]^3 |F_p(q^2)|^2 = [QED]\cdot|F_p(q^2)|^2 \tag{1.20}$$

From general considerations the influence of the form factor can either increase the leptonic pair spectrum, as compared with that obtained for point particles, or decrease it. To estimate the order of magnitude and sign of the expected effect, one may use the VDM hypothesis described in the previous section.

In the VDM, the transition form factors in meson conversion decay are described according to the diagrams in Figure 1.2.

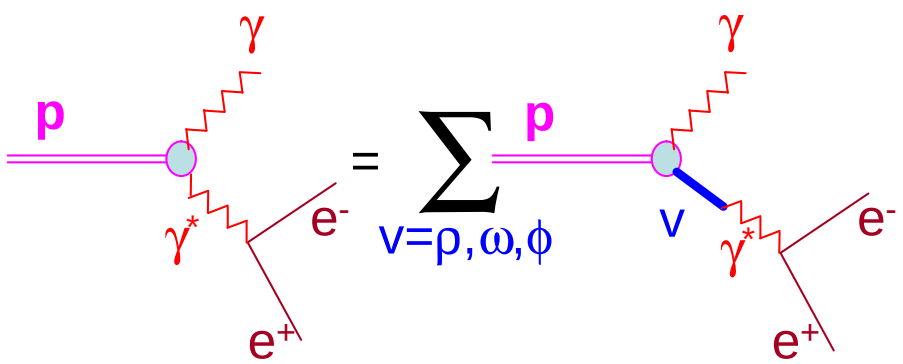

Figure 1.2: Diagrams for the transition form factor of the pseudoscalar meson in the VDM.

In order to test the validity of the VDM model in describing the η meson decay, the reconstructed invariant-mass spectrum of e^+e^- pairs coming from η Dalitz decay ($\eta \rightarrow e^+e^-\gamma$) will be compared with the VDM calculations in this work.

1.3 Previous measurements

1.3.1 η meson form factor

Only two measurements of the η meson form factor has been performed so far. One of them was done for the $\eta \to \mu^+\mu^-\gamma$ decay channel which puts a constraint from lower part of the distribution due to the mass of the muon as shown in Figure 1.3[2]. Nevertheless as it is seen from the Figure the VDM model (dashed curve) describes the data quite well in the allowed region. In the Figure the form factor is measured as a ratio of effective mass spectrum of di-muons to the QED calculations (see Equation 1.18). The solid line in the Figure corresponds to the fitting of the experimental data with:

$$F_\eta(q^2) = \left(1 - \frac{q^2}{\Lambda_\eta^2}\right)^{-1} \tag{1.21}$$

where $\Lambda_\eta = 0.72 \pm 0.09 GeV$.

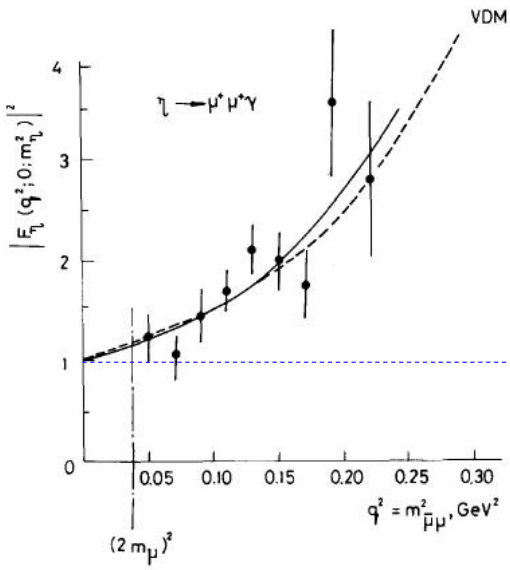

Figure 1.3: Data on the η meson transition form-factor. The points are experimental values [2]. The solid line is the result of fitting the experimental data points with formula 1.21. The dashed curve is the VDM prediction. A point-like η meson would imply that the the data follow the blue dashed line.

The another measurement had been performed for $\eta \to e^+e^+\gamma$ with poor statistics (50 counts) [7].

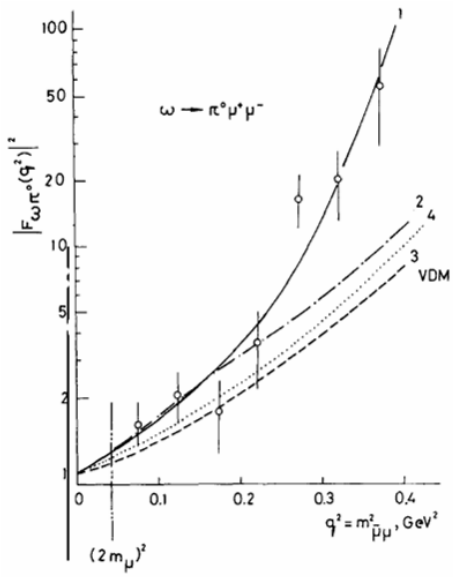

Figure 1.4: Data on the transition form-factor for the $\omega\pi^0$ vertex [2]. The solid line is the fit of the experimental data points with formula 1.22. Curve 3 has been calculated with the VDM.

The VDM model fails to explain the decay of the ω meson. The data obtained for $\omega \to \pi^0\mu^+\mu^-$ is shown in Figure 1.4 [2]. Line 3 in the Figure corresponds to the VDM model which clearly does not describe the data. Line 1 in the Figure corresponds to the parametrization of the experimental data with:

$$|F_{\omega\pi^0}(q^2)|^2 = \left(1 - \frac{q^2}{\Lambda_\omega^2}\right)^{-2} \tag{1.22}$$

where $\Lambda_\omega = 0.65 \pm 0.03 GeV$.

1.3.2 η meson production

At CELSIUS [8], angular distributions of the η emission in the center-off-mass system has been measured in proton-proton collisions at near threshold energies (excess energies $Q = \sqrt{s - s_0}$ =16 and 37 MeV). It has been shown that the η differential cross section as a function of the η polar angle in center-of-mass frame is not isotropic and shows a maximum of emitted η mesons perpendicular to the beam direction.

The angular distribution measurement at COSY [9] at similar excess energies shows, however, no deviation from isotropy, which is in contradiction to the measurements at CELSIUS.

Exclusive measurement of the η mesons in proton-proton collisions at the beam kinetic energies of 2.15 GeV, 2.50 GeV, and 2.85 GeV had been performed by the DISTO experiment [10]. It was observed that, angular distributions of differential cross section indicates the polar angle anisotropy of the η meson in the center-of-mass system. Furthermore these investigations have shown that the anisotropy gradually vanishes with increasing beam energy.

The anisotropy in angular distributions of the η mesons observed by the DISTO experiment has been included in our simulation [11] and compared with the reconstructed one from experimental data.

1.4 Vector mesons in hadronic matter

Major part of the HADES physics program is focused on in-medium properties of the light vector mesons $\rho(770)$, $\omega(783)$ and $\phi(1020)$. The in-medium properties of the vector mesons in hot and dense matter play an important role in the low-mass dilepton production resulting from heavy-ion collision experiments. This has, hence, been a topic of great interest in recent past, both experimentally [12, 13, 14, 15, 16] and theoretically [17, 18, 19, 20, 21].

Such investigations can be done by studying the proton-nucleus, pion-nucleus and heavy-ion collisions.

In particular, the short-lived ρ meson is an ideal candidate for such studies. The mean life time of the ρ meson, $c\tau \approx 1.5fm$, is shorter than the fireball lifetime, thus allowing to explore decays inside the hot and/or dense nuclear matter. In-medium modifications of the ρ properties should be reflected in dielectron invariant mass distribution.

Chapter 2

HADES detector system

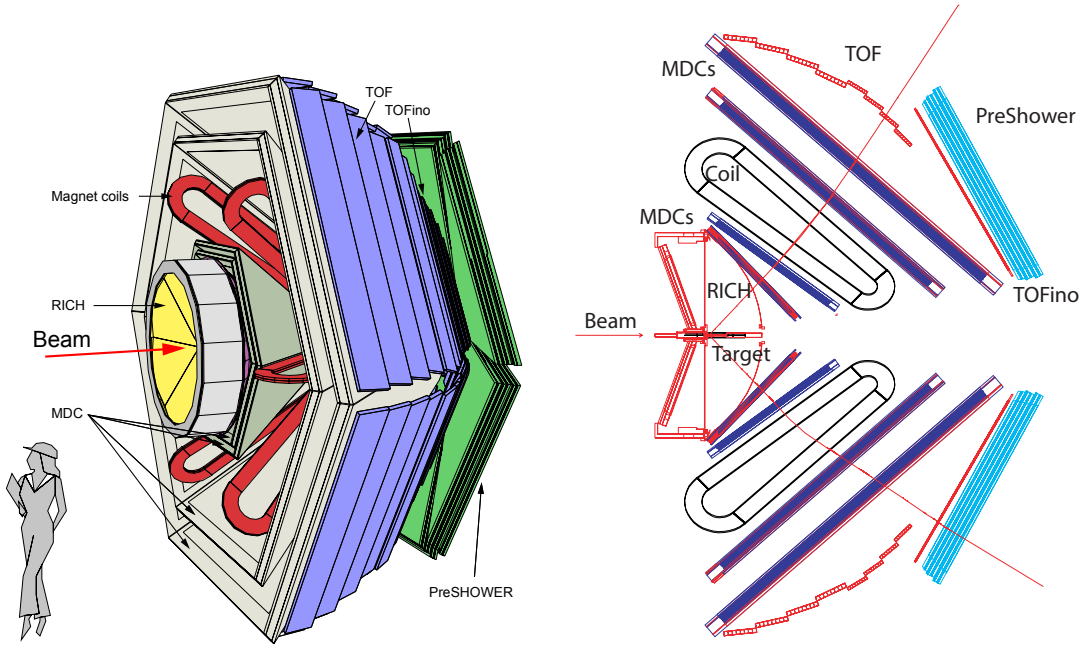

(a) 3-D view (b) Side view

Figure 2.1: The HADES spectrometer (a) 3-D view and (b) side view.

The main goal of detector systems is to deliver several information about a particle:

- energy E (or the momentum p) of the particle at some defined point.
- Identification of the particle, thus defining its mass and charge.
- The coordinates of point on the track together with directions at those points.

Using these information it is possible to calculate a particle's energy at any point of its trajectory, and particularly at the point of interaction.

The main goal of the HADES experiment is to investigate decays of vector mesons via the dilepton decay channel. These decay channels of the vector mesons are suppressed by a factor of $\approx 10^{-5}$ as compared to the hadronic decays. In order to accumulate significant statistics in a reasonable time, the HADES spectrometer design should meet several conditions [22]:

- Large geometrical acceptance in order to maximize the probability of detecting a pair once it is produced.
- High rate capabilities allowing for an operation at beam intensities of up to 10^8 particles/s.
- The high interaction rate together with high hadron multiplicity resulting from the large acceptance represents a serious challenge to the trigger system which has to filter out events containing lepton tracks.
- Sufficient granularity on detectors, so that it is possible to deal with high particle multiplicities.
- The pair mass resolution has to be sufficient to detect changes of the in-medium width of the ω and ϕ mesons. The pair mass resolution should therefore be comparable to the natural width of these states which is about 1%. This requirement subsequently sets conditions on single trajectory momentum resolution as well as on the determination of position which is used for the reconstruction of the momentum of the particles and the pair opening angle. Therefore a magnetic spectrometer is needed with high position resolution before and after the magnetic field.

The HADES spectrometer is a rotationally symmetric, large acceptance toroidal spectrometer with a complete azimuthal coverage [22, 23, 24]. The spectrometer acceptance in polar angles covers the $18^0 - 85^0$ range. The achieved geometrical acceptance of $\sim 40\%$ represents an improvement by a factor of 100 as compared to the pioneering experiments performed with the DLS spectrometer at Berkeley [13].

The HADES detector system consists of the following sets of detectors:

- Start and Veto detectors
- Ring Imaging Cherenkov detector (RICH)
- Magnet
- Multi wire Drift Chambers (MDC)

- Time Of Flight detectors (TOF) and (TOFINO)
- Pre-Shower detectors (SHOWER)

2.1 Start and Veto detectors

The START and VETO diamond detectors are two identical octagonal shaped diamonds synthesized using the Chemical Vapor Deposition (CVD) technique [25]. The thickness of the detector is 100μm to minimize multiple scattering. The START detector, as well as the VETO, both have dimensions of 25mm$\times$15mm, and placed 75cm upstream and downstream of the target position, are segmented into 8 strips and work in anti-coincidence, such that when a beam particle crosses without interacting with the target it provides a signal in the VETO detector as well and the corresponding event is vetoed. The width of the strips is optimized to guarantee 96.5% VETO efficiency. The START and VETO detectors are used to give a start to the time measurements.

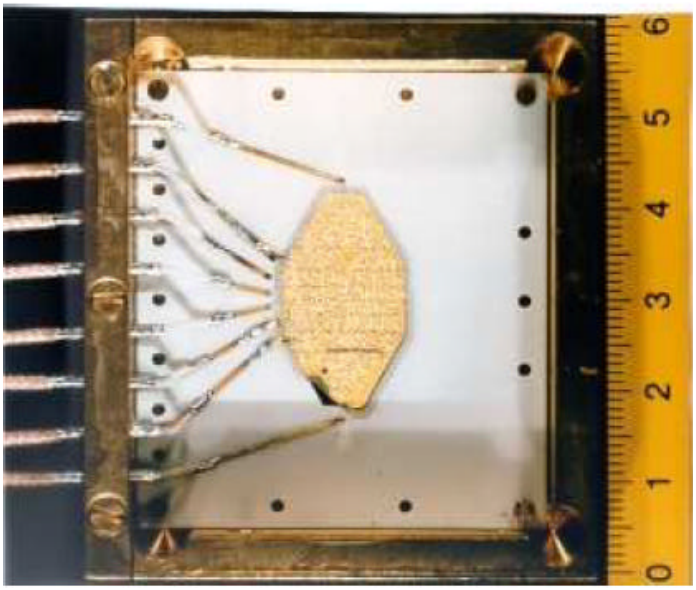

Figure 2.2: The diamond START detector. The VETO detector is identical.

The diamond detectors were not used for proton beams, because the energy loss inside the START material is so small that is does not produce a useful signal. Therefore for the proton beams a pair of scintillating hodoscopes were tested in a commissioning run.

Due to the large number of secondaries produced in proton interaction with the detectors it was decided not to use any START detector for the proton production run. The data

acquisition was started by a fastest particle which crossed the TOF/TOFINO walls and produced a signal above threshold. Therefore during this run the TOF/TOFINO system was measuring the difference between particle's time-of-flight and the time-of-flight of the particle which triggered the data acquisition. The start time of the reaction was reconstructed using an algorithm based on assigning a theoretically calculated time of flight to the identified particle[1]. The difference between a theoretically calculated value of time-of-flight (t_{th}) and the experimental one (t_{exp}) allows one to calculate the start time of the reaction (t_0)

$$t_0 = t_{th} - t_{exp} \tag{2.1}$$

The reconstructed start time in this way should be added to the measured time of the the other particles inside the same event to obtain the corrected time-of-flight. This procedure is performed on event-by-event basis.

2.2 Ring Imaging Cherenkov Detector

In 1934 P. A. Cherenkov observed a new radiation with the following properties [26, 27]:

- The polarization of the radiation changes under influence of a magnetic field. This means the radiation is induced by charged particles.
- The radiation intensity is independent of the medium charge Z that is why it cannot not be of radiative origin
- The radiation is emitted along certain direction.

This radiation later on was explained by I.E. Tamm and I.M. Frank within classic electrodynamics [28]. According to classical electrodynamics a uniformly moving charged particle in a vacuum cannot lose its energy due to radiation, but one can easily deduce based on the energy-momentum conservation laws that this can happen when particle moves through a medium if its velocity is greater than the phase velocity of light in the medium.

The emission of Cherenkov radiation is based on coherent radiation of dipoles created in a medium by the field of the passing particle. When a particle traverses with a relatively small speed it polarizes the medium around it in a symmetric way that is why the net radiation from all dipoles will cancel each other.

[1]The negative particle was assumed to be an electron if there was a matching with the signal from the RICH detector or a negative pion in the other case.

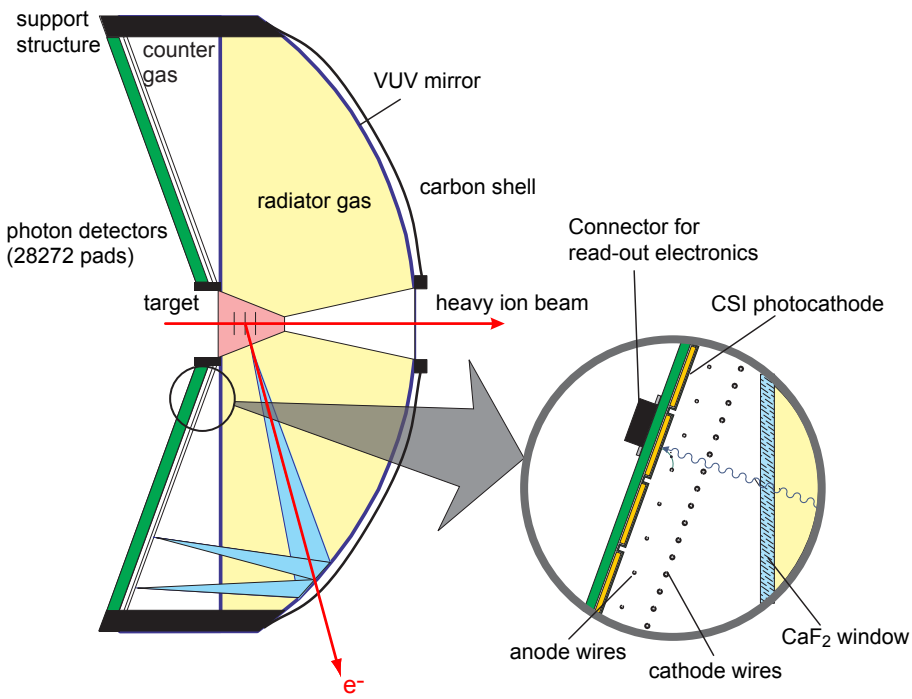

Figure 2.3: The Ring Imaging Cherenkov detector.

On the other hand in case of high speed particle there will be so called polarization delay effect of the medium resulting in polarization mainly in the direction of particle motion. In this case there can be coherent radiation of created dipoles in some direction. The coherent wave front formed is conical and is emitted at an angle

$$\cos\theta = \frac{1}{\beta n} \tag{2.2}$$

with respect to the trajectory of the particle.

This physics is used in the HADES **R**ing **I**maging **C**herenkov **D**etector (RICH) for lepton identification. The particle is identified if $\beta \geq 1/n$, therefore

$$\gamma \geq \sqrt{\frac{n^2}{(n^2-1)}} \tag{2.3}$$

The RICH is the main component of the HADES spectrometer for a lepton identification [29, 30]. It consists of a C_4F_{10} gaseous radiator surrounding the target located roughly in the focal point f=R/2 of a spherical mirror with radius of R=87.1 cm and a position sensitive Photon Detector (See Figure 2.3). The radiator gas has an index of refraction

n=1.00151, which corresponds, according to Equation 2.3, to a threshold of $\gamma_{thr} \approx 18.3$ and guarantees the hadron blindness of the detector. Indeed, the threshold energies to emit a Cherenkov light in such a medium are therefore 15.9 GeV for protons, 2.4 GeV for pions, far above the SIS energies, while for electrons it is 8.5 MeV which is well below the range of interest.

Electrons with velocities $\beta \approx 1$ radiate a Cherenkov light in a cone along their tracks through the radiator. The light is reflected by the aluminized carbon fiber mirror and is focused as an elliptical image on the position sensitive Photon Detector, which is separated by a 5 mm CaF_2 window from the radiator volume. The Photon Detector is composed of Multi Wire Proportional Chambers with a segmented photocathode. When Cherenkov photons reach the photocathode, electrons are emitted by photoelectric effect, induce an electric charge on the photocathode, in one (or more neighboring) pads it is segmented into.

2.2.1 Energy loss of charged particles

Charged particles other than electrons lose energy in matter primarily by ionization and atomic excitation. The mean rate of energy loss (or stopping power) is given by the Bethe-Bloch equation,

$$-\frac{dE}{dx} = Kz^2 \frac{Z}{A} \frac{1}{\beta^2} \left[\frac{1}{2} ln \frac{2m_e c^2 \beta^2 \gamma^2 T_{max}}{I^2} - \beta^2 - \frac{\delta}{2} \right] \tag{2.4}$$

with K/A=$4\pi N_A r_e^2 m_e c^2/A$=$0.307075\ MeV g^{-1}\ cm^2$ for A=1 $g\ mol^{-1}$

r_e:	classical electron radius=2.817$\times 10^{-13}$cm
N_A:	Avogadro's number=6.022$\times 10^{23} mol^{-1}$
m_e:	electron mass
I:	mean excitation potential
Z:	atomic number of absorbing material
A:	atomic weight of absorbing material
z:	charge of incident particle in units of e
β=	v/c of the incident particle
γ=	$1/\sqrt{1-\beta^2}$
δ:	density correction
T_{max}:	maximum energy transfer in a single collision

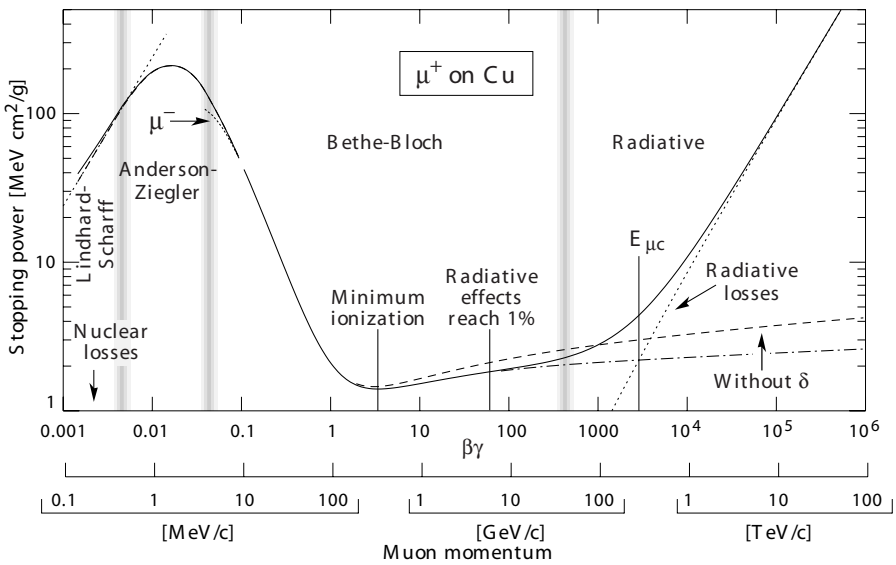

Figure 2.4: Stopping power (=$< -dE/dx >$) for positive muons in copper as a function of $\beta\gamma = p/Mc$.

An example of the energy dependence of dE/dx is shown in Figure 2.4 [31] for muons on copper. As $\beta\gamma$ is increased dE/dx falls at first with $1/\beta^2$ factor, then goes through a minimum. Particles at this point are known as minimum ionizing. The minimum value of dE/dx is almost the same for all particles of the same charge. As the $\beta\gamma$ increases beyond this point, the term $1/\beta^2$ becomes almost constant and dE/dx rises again due to the logarithmic terms in 2.4, describing a relativistic rise. It was discovered later that the relativistic rise would not continue infinitely due to the ”density effect”, calculated by Fermi. A corresponding correction term δ is introduced into Equation 2.4 [28, 32].

Ionization detectors were the first electrical devises developed for radiation detection. These instruments are based on the direct collection of the ionization electrons and ions produced in a gas by passing radiation.

Because of the greater mobility of electrons and ions, a gas is the obvious medium to use for the collection of ionization from radiation.

We distinguish between primary and secondary ionization. The electrons and ions created by the incident radiation itself are known as a primary ionization. In primary ionization, one or sometimes two or more electrons are ejected from the atom X encountered by a fast particle p,

$$X + p \rightarrow X^+ + p + e^- \tag{2.5}$$

Most of the charge along a track is from secondary ionization where the electrons are

ejected from atoms not encountered by the passing particle. This happens either in collisions of ionization electrons with atoms, or through intermediate excited states X^*.

Multiplication in gas detectors occurs when the primary ionization electrons gain sufficient energy from the accelerating electric field to also ionize gas molecules. The resulting secondary electrons then produce an ionization and so on. This results in the formation of an avalanche. The pulse signal is created on the electrodes due to the movement of the ions and electrons as they drift towards the cathode and anode. Spatial information can be obtained by measuring the drift time of the electrons coming from an ionizing effect.

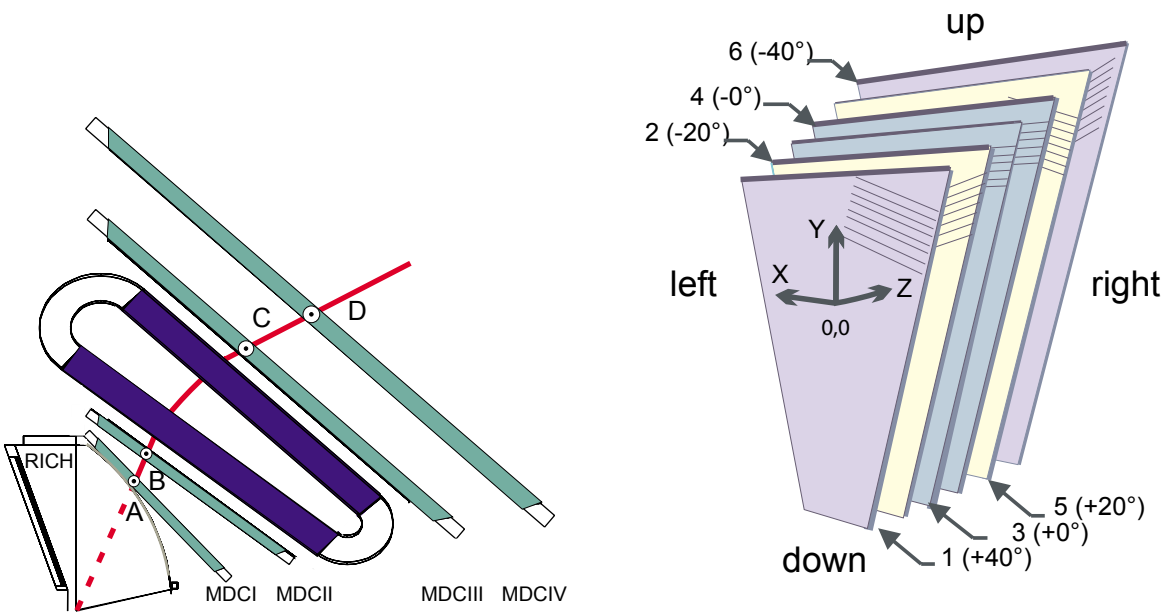

(a) (b)

Figure 2.5: Arrangement of MDC chambers with respect to magnet coils (a) and arrangement of sense wires in different layers of one MDC (b).

2.2.2 HADES tracking system

The physics described in the previous section makes the basics of operation of a **M**ulti wire **D**rift **C**hambers (MDC), the main tracking part of the HADES experiment [32].

There are in total 24 MDCs, of trapezoidal shape, symmetrically arranged in six identical sectors. They provide a polar angle coverage between 18^0 and 85^0 around the beam axis, forming four tracking planes (I-IV) of increasing size. In each sector, two chambers (plane I and II) are located in front of, and two (plane III and IV) behind, the toroidal magnetic field of the super-conducting magnet, as shown in Figure 2.5(a). To cope with

ambiguities (left right ambiguity) in track reconstruction in the high multiplicity environment of a heavy ion reaction, all chambers are composed of six sense/field wire layers oriented in five different stereo angles and seven layers of cathode wires. The cathode wires are oriented perpendicular to the top and bottom frames of the MDCs [33, 34].

This arrangement of wire layers allows for maximum spatial resolution in polar directions, which points in the direction of the momentum kick. From geometrical point of view the two potential wires, the sense wire being in between, together with the cathode wires form a drift cell. The field and cathode wires are made of bare aluminium, with diameters of 100 μm and 80 μm respectively. The sense wires are made of gold plated tungsten with a diameter of 20 μm. All four chamber types contain about 1100 drift cells each, with increasing size, from 5×5 mm^2 (plane I) to 14×10 mm^2 (plane IV), to maintain the granularity per solid angle.

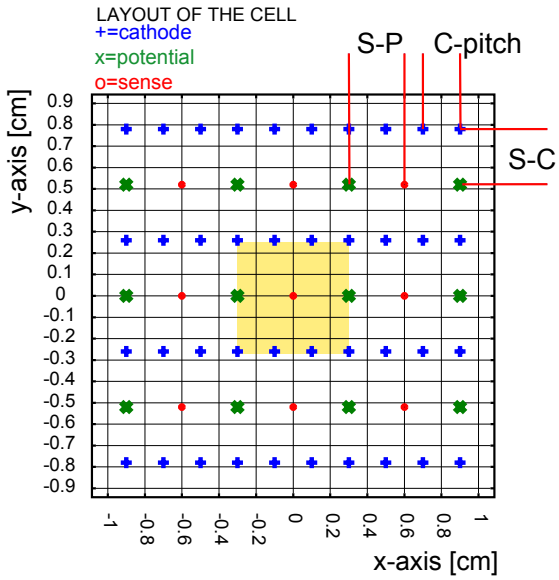

Figure 2.6: Geometry of a drift cell for MDCII. The position of the cathode wires are labeled with +, the sense wires with **0**, and the potential wires with **x**. The yellow area marks the drift cell.

A particle passing the drift cell ionizes the counting gas. The ionization is statistically distributed along the track, initiates separate clusters of electron clouds drifting towards the sense wire and triggers the signal picked up by a fast amplifier connected to the wire. This signal gives the start of the time measurement. The stop is deduced from an external detector e.g. delayed trigger of the start detector. The resulting arrival time of the electrons, after time offset subtraction and calibration of the TDC slope is converted into a distance from sense wire to the point of closest approach of the trajectory.

In the HADES experiment the drift cells are modeled in a two dimensional representation. In the model the cathode wires are parallel to the sense and potential wires. The model of the drift cell is shown in Figure 2.6. The drift cells are investigated using the simulation program GARFIELD [35], which is capable of electric and magnetic field computations of two dimensional geometries.

Using GARFIELD simulations, to each position of the track in space in terms of impact angle to the cell and closest distance to the sense wire of the cell the calculated value of the drift time and its error is assigned (*xt* relation) (See Figure 2.7).

In order to achieve a mass resolution better than 1% in ρ/ω mass region the drift cells have to provide a position resolution of better than 140 micron. Therefore, both the in-

trinsic position resolution of the drift chambers as well as the multiple scattering along the spectrometer play a key role. Multiple scattering is dominant at low ($< 0.4GeV/c^2$) dilepton invariant mass. The use of the Helium as the main counter gas is mandatory to keep the contribution of the multiple scattering at tolerable level, because its radiation length is almost 50 times longer that of Argon. The lack of total primary ionization of Helium is usually compensated by using iso-butane as quencher. Several small and one full size prototypes of MDCs have been built and tested for different concentrations of iso-butane in Helium. From these investigations it was concluded that the mixture containing 40% iso-butane is the optimal choice for application, because it provides enough primary ionization statistics under stable operation at moderate gains [36].

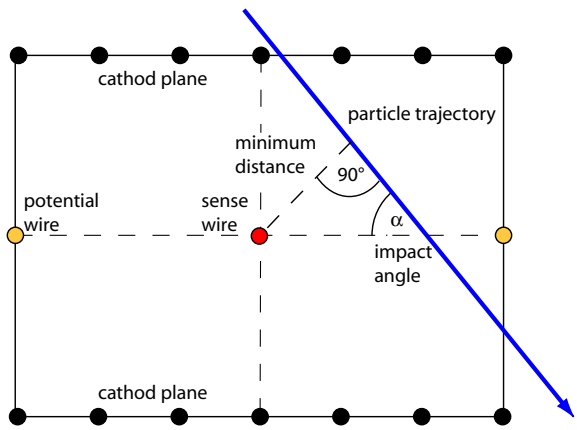

Figure 2.7: Two dimensional coordinate system of the parametrization of a particle track in GARFIELD. The parametrization of the track is based on the minimum distance to the sense wire and the impact angle of the track to the drift cell.

2.3 Magnet

The magnetic field should fulfill several requirements:

- It must deflect charged particles such that their momenta can be obtained with sufficient resolution.
- There should be nearly field free region in the RICH detector.
- Large momentum range must be accepted simultaneously within a large solid angle.

The HADES magnet consists of six super-conducting coils surrounding the beam axis producing the toroidal field. Each coil consists of a straight entrance and exit section

connected by two arcs. The angles of the entrance and exit sections of 40^0 and 45^0 with respect to the beam line were chosen to minimize the azimuthal deflection of particles over the whole polar angular range from 18^0 to 85^0.

Figure 2.8 shows contour plots of the main magnetic field component at azimuthal angles of $\phi = 90^0$, $\phi = 75^0$ and $\phi = 60^0$. The maximum field of 3.7T is obtained at the coil surface inside the forward arc. In between the coils, i.e., at the azimuthal angle of 90^0, the filed extends over a wider region as compared to the azimuthal angle of 60^0 which is close to the coil.

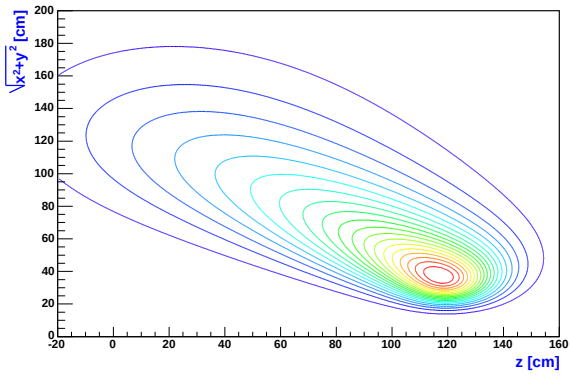

(a) $\phi = 90^0$

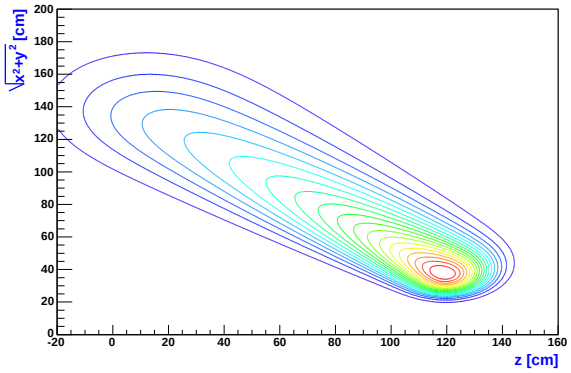

(b) $\phi = 75^0$

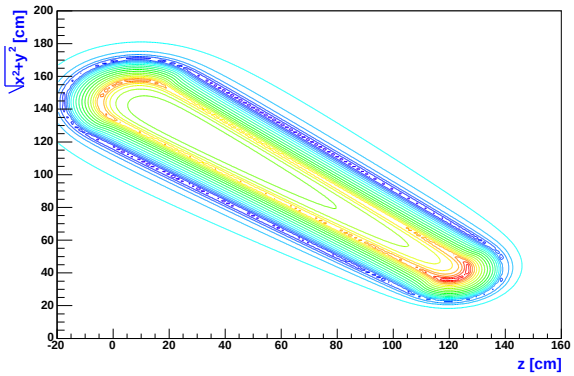

(c) $\phi = 60^0$

Figure 2.8: Contour plots for the main component of the magnetic field at different azimuthal angles.

2.4 Multiplicity Electron Trigger Array (META)

The META is positioned behind the outer MDCs and is used for particle identification by measuring the time between start detector signal and arrival time. It is used for triggering

purpose as well. The META consists of two Time of Flight systems, an outer TOF and inner TOFINO, covering the full HADES acceptance and the Pre-Shower gas chambers at forward polar angles $\theta < 45^0$.

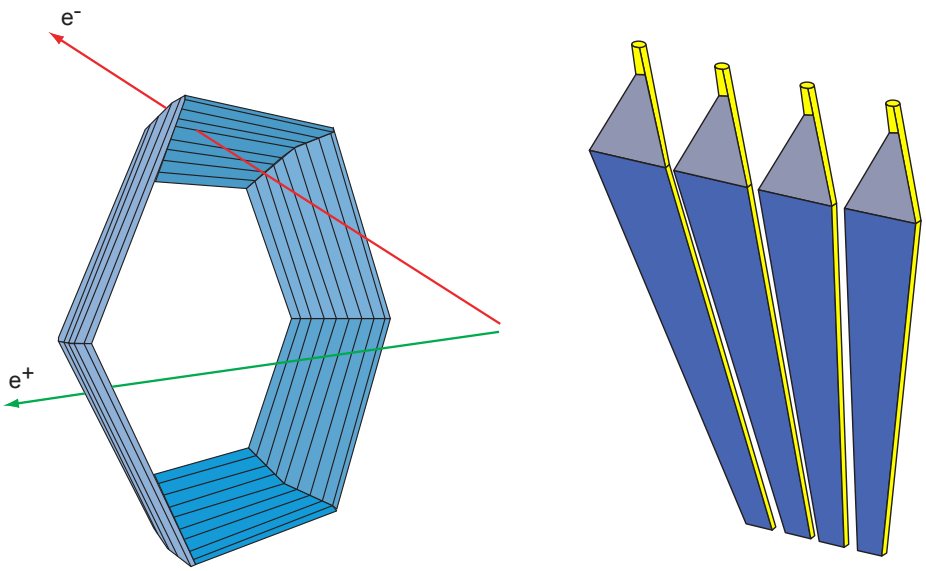

(a) TOF (b) TOFINO

Figure 2.9: TOF (a) and TOFINO (b) detectors.

2.4.1 TOF and TOFINO detectors

Certain materials when struck by a nuclear particle or radiation, emit a small flash of light, i.e. a scintillation. The scintillator detector is undoubtedly one of the most often and widely used particle detection devices in nuclear and particle physics today. The TOF detector follows the hexagonal geometry of the whole spectrometer, and consists of 8 modules per sector each of them being composed of 8 scintillator rods (therefore 64 bars per sector) connected from both sides to photomultiplier tubes [37]. When hit by a particle it provides the light signal which is collected at both ends and then converted to time signal by a TDCs (Time-to-Digital Converter). By combining this information one can extract time-of-flight and hit position of the particle.

If the t_l and t_r are times measured by the left and right TDCs we can write,

$$\begin{aligned} t_l(x) &= tof + \tfrac{1}{V_g}\left(\tfrac{L}{2} + x\right) \\ t_r(x) &= tof + \tfrac{1}{V_g}\left(\tfrac{L}{2} - x\right) \end{aligned} \tag{2.6}$$

where tof is the time of flight of the particle, V_g is the group velocity of the light in the scintillator material, L is the length of the rod, and x is the distance between the center of the rod to the point where the particle hits the rod.

From two equations in 2.6 we find:

$$\begin{aligned} tof &= \tfrac{t_r(x)+t_l(x)}{2} + t_{offcet} \\ x &= \tfrac{t_r-t_l}{2} V_g \end{aligned} \tag{2.7}$$

where

$$t_{offcet} = -\frac{L}{2V_g} \tag{2.8}$$

Using time of flight information it is possible to distinguish electrons from protons and pions or pions from protons up to some momentum range.

For time of flight measurements the region of polar angles $\theta < 45^0$, is currently covered by a low granularity system called TOFINO. It is divided into six sectors, and each sector is made of four scintillator paddles, arranged radially with respect to the beam axis as shown in Figure 2.9(b). The operation principle of the TOFINO wall is similar to the TOF detector, but in this case the light is collected only at one edge of the scintillator pad. Therefore using only TOFINO information it is not possible to have the position information of the hit. The position information in this case is defined by correlation with the SHOWER detector.

2.4.2 Pre-Shower Detector

Particles passing through matter are scattered and lose energy by collisions. Under these collisions the particles undergo acceleration, hence they emit electromagnetic radiation. The radiation emitted during atomic collisions is customarily called bremsstrahlung (braking radiation) because is was first observed when high energy electrons were stopped in a thick metallic target. For non-relativistic particles the loss of energy by radiation is negligible compared with the collisional energy loss, but for ultra-relativistic particles radiation can be the dominant mode of energy loss. The energy loss is proportional to the square of acceleration. It is clear that Coulomb forces (F) between particles of equal charges (z) and nuclear are the same, hence

$$[(\ddot{x})^2 \sim \frac{1}{m^2}]_{z=const} \tag{2.9}$$

therefore,

$$[(\frac{dE}{dx})_{radiation}]_{z=const} \sim \frac{1}{m^2} \tag{2.10}$$

So, radiative losses for particles of equal charge are inversely proportional to the squared masses; bremsstrahlung therefore plays a particularly important role for light particles.

For each material a critical energy is defined where the average energy loss by ionization and radiation are the same and hence for the electrons above critical value the main mechanism for energy loss is a radiation one.

The combined effects of bremsstrahlung and pair production by an emitted photon produces the so called electromagnetic shower: a high energy electron emits by bremsstrahlung a photon which then by conversion produces an electron- positron pair; electron and positron emits again photons and so on, resulting in a cascade of electrons, positrons and photons.

The HADES Pre-Shower detector uses this effect to distinguish electrons, which develop such a shower, from pions which do not, in the region of small polar angles. Pre-Shower modules are mounted together with four TOFINO paddles in six azimuthally symmetric sectors. The side view of the Pre-Shower detector is shown in Figure 2.10.

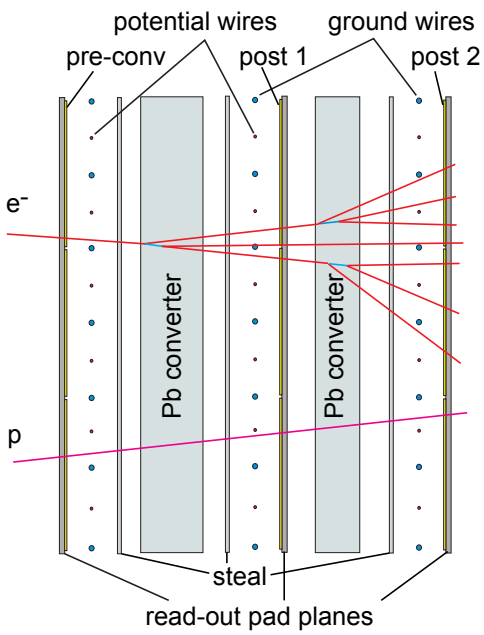

Figure 2.10: Side view of the Pre-Shower detector.

It is composed of a stack of three wire chamber layers (pre-converter, post1-converter, post2-converter) [38]. Each chamber is filled with an argon-isobutan mixture and contains one wire plane and two flat cathodes. In between the planes there is a layer of lead converter with a thickness of almost 1cm. One cathode plane is divided into pads of varying dimensions with an individual signal red-out while the other cathode plane is a flat stainless steel plate. A charged particle passing through the chamber produces an avalanche

of electrons drifting towards the closest anode wire. The avalanche current induces the current of positive polarity on adjacent cathode pads. It is integrated into charge afterwards. The chambers operate in a Self-Quenching Streamer mode which guaranties that the collected charge depends only weakly on the particle specific energy loss [39]. The integrated charge is proportional to the number of particles which enter the chamber. The electromagnetic shower recognition algorithm is based on direct comparison of the integrated charges on corresponding areas of the pre-converter and the post1/post2-converter planes. The integration area has been limited to 3×3 pads.

2.5 HADES trigger system

Since the branching ratio for dilepton decays of vector mesons is on the order of $10^{-5} - 10^{-6}$, in order to collect enough statistics an online selection trigger is needed.

The resulting rate of the nuclear reactions which might reach the spectrometer, for the beam intensities of $10^8/s$, is of the order of 10^6 events per second for the target thickness of 1% interaction length. The maximal limit of $10^5/s$ was taken as an upper limit for the trigger design.

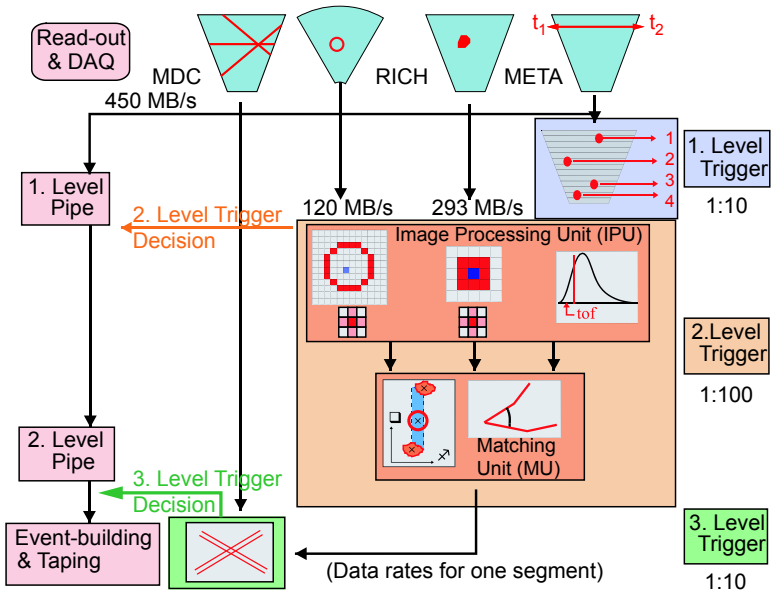

Figure 2.11: Hades trigger system.

The first level trigger (LVL1) selects the most central collisions, based on the multiplicity of charged particles collected in TOF and TOFINO detectors and reduces the event

rate by a factor of 10, down to 10^5 events per second.

The aim of the HADES second level trigger (LVL2) is to perform fast dielectron identification in the RICH and META Image Processor Units (IPU) and to limit data written on tape to events with at least one electron candidates. The LVL2 trigger performs a two step process shown in Figure 2.11. In the first step a search for electrons ring images on the RICH pad plane, charge clusters with the signature of electromagnetic cascade in the Pre-Shower detector and hits with appropriate time of flight in the TOF detectors is done. In the second step a Matching Unit (MU) correlates the position coordinates of electron candidates in RICH and META detectors taking into account the deflection due to the magnetic field [40].

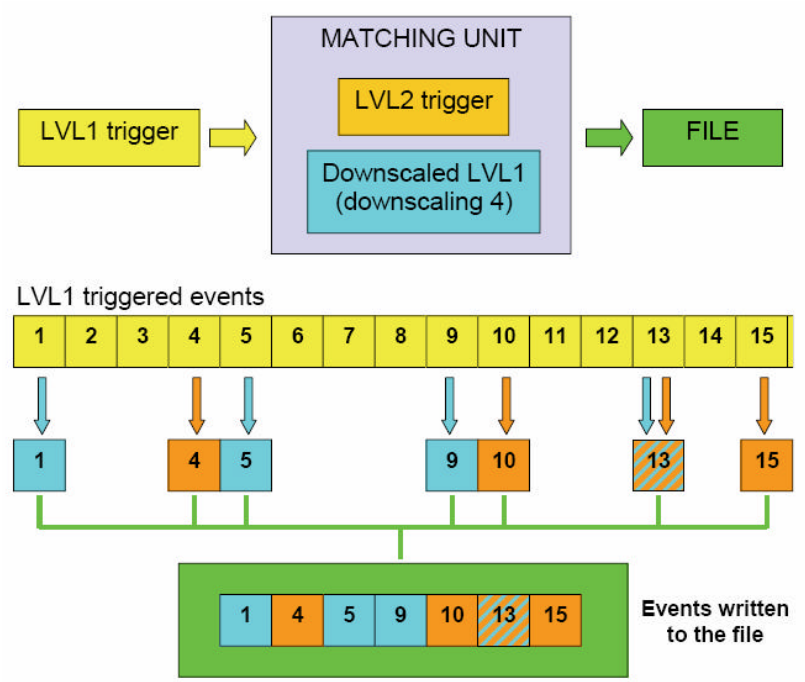

Figure 2.12: Event selection scheme used for data acquisition.

All the events which pass 1st level trigger decision are sent to the matching unit board, which decides whether the event has to be accepted or discarded. This decision is taken separately by two different systems which operate independently: the downscaling box and the 2nd level trigger itself. The 2nd level trigger selects events which contain a lepton candidate, according to the information from IPU; all these events are stored into the data file. We call them LVL2 events.

However, we do not want to acquire only the events with lepton pairs, but also events which contain only hadrons; if we would record all the 1st level triggered events without

any further scaling, the stored data will be dominated by hadronic reactions.

The downscaling box purpose is to select and scale down events in a statistical fashion, regardless of whether they contain lepton pairs or not. In this case we talk about downscaled events.

Figure 2.12 represents a scheme of the event selection used for data acquisition. A first selection of events is done by the 1st level trigger (yellow boxes), and they are sent to the matching unit, where the downscaling factor is set to 4. This means that one event out of four is stored (1,5,9,13,...), regardless of the 2nd level trigger decision. It is flagged as downscaled in the event header and the related downscaling factor is stored as well. All the events with a recognized lepton are stored as well, and flagged as LVL2. This means that an event can be at the same time downscaled (LVL1) and with positive 2nd level trigger decision (LVL2) like for instance the event number 13 in the example.

If we want to have the total number of 1st level triggered events, we must multiply the number of downscaled events (4) by the downscaling factor (4); in this case we obtain 16 triggered events, against 7 which are effectively stored to file. In this particular case we are roughly saving half of the disk space, and half of the time needed for the data acquisition.

In fact 2nd level trigger has an efficiency below 100%, therefore in evaluating the number of dilepton events in the data sample this correction has to be taken into account.

Chapter 3

HADES Tracking

In this section the tracking algorithm of the HADES spectrometer is described. The tracking procedure consists of several steps: track finding, track fitting and momentum reconstruction. For the momentum reconstruction, different methods have been developed described in the following sections.

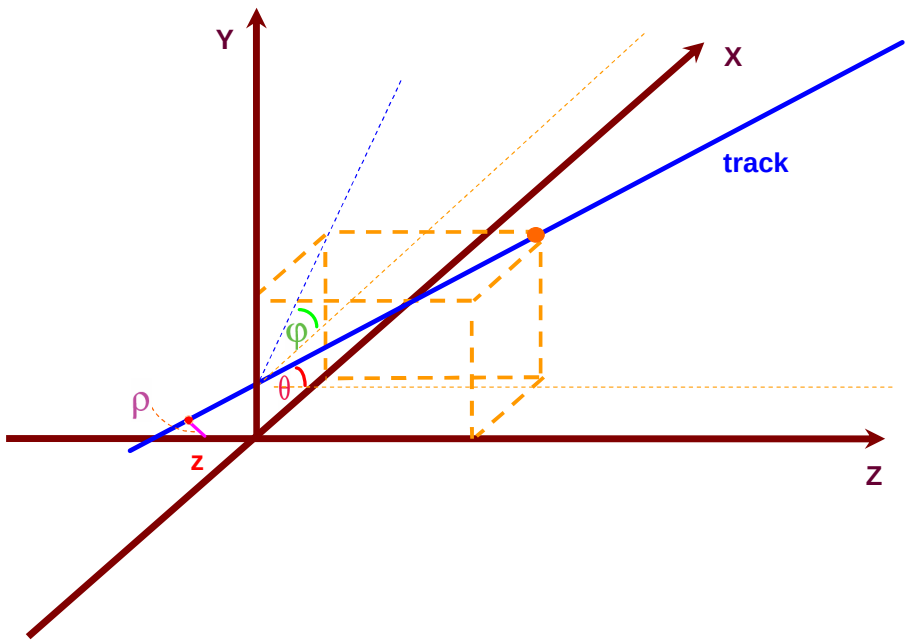

Figure 3.1: Track parametrization (θ, ϕ, ρ, z) in the HADES experiment.

3.1 Track parametrization in the HADES experiment

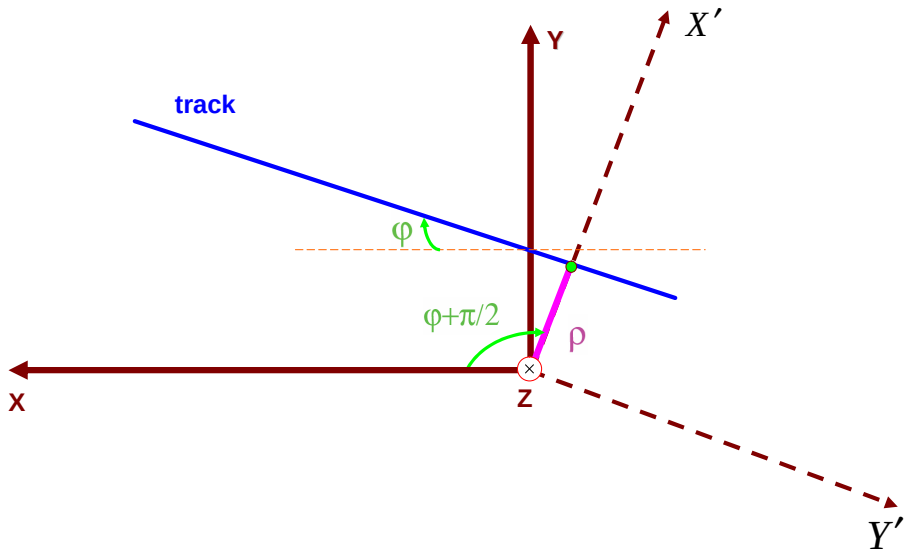

Figure 3.2: The track viewed along the z axis. The beam is directed perpendicular to Figure plane, along z axis.

In the HADES experiment a track is parameterized with four variables in the sector coordinate system:[1] : θ , ϕ , ρ and Z. Here θ and ϕ are polar and azimuthal angles correspondingly, ρ is a distance between the z axis and a closest point of the track to that axis, and Z is the z coordinate of that point. Let us assume the x and y coordinates of the closest point on the track to z axis to be X and Y (See Figure 3.2 (the z axis is perpendicular to the Figure plane)). In the Figure the blue line represents the track while the pink line shows the closest distance from the track to the z axis looked at in the direction of the z axis. It can easily be seen from Figure 3.2 that, if we rotate our coordinate system around z axis by an angle $\phi + \pi/2$, which can be realized by the following rotation matrix:

$$\begin{pmatrix} \cos(\phi+\pi/2) & \sin(\phi+\pi/2) \\ -\sin(\phi+\pi/2) & \cos(\phi+\pi/2) \end{pmatrix} \tag{3.1}$$

in the new coordinate system (X',Y') the ρ vector will be along the X' axis with its module being equal to $\sqrt{X'X'}$; therefore the x coordinate of the closest point will be just

[1]In the Hades experiment a left-handed coordinate system as illustrated in Figure 3.1 is used. Sector coordinate system means that the system is attached to the sector. In this coordinate system the ϕ angle ranges between 60^0 and 120^0. It is just rotated with respect to the LAB coordinate system by an angle n*60^0 where n stands for the sector number.

just to the module of the closest distance (ρ), while the y coordinate will be equal to 0, which can be written using the above transformation matrix:

$$\begin{cases} \rho = X * \cos(\phi + \pi/2) + Y * \sin(\phi + \pi/2) \\ 0 = -X * \sin(\phi + \pi/2) + Y * \cos(\phi + \pi/2) \end{cases} \tag{3.2}$$

Solving equations 3.2 one can easily obtain:

$$\begin{cases} X = \rho * \cos(\phi + \pi/2) \\ Y = \rho * \sin(\phi + \pi/2)) \end{cases} \tag{3.3}$$

The next step is to obtain the directions, for instance, by taking the unit radius sphere around (X, Y, Z) point.

$$\begin{cases} dirX = \sin(\theta) * \cos(\phi) \\ dirY = \sin(\theta) * \sin(\phi) \\ dirZ = \cos(\theta) \end{cases} \tag{3.4}$$

3.2 Track reconstruction algorithm

The main purpose of the tracking algorithm is to find the four parameters described in the previous section which define the orientation of the track pieces (segments) in space before and after the MAGNET belonging to a given track. Furthermore, using the information from track bending inside the magnetic field, the momentum of the track is calculated as well. The HADES track reconstruction algorithm consists of several steps:

- Track finder
- Track fitter
- Momentum reconstruction

In the track finder the initial position of the track is found using only geometrical considerations which serves then as an input to the track fitting.

The track fitting algorithm improves the parameters found by the track finder by changing the track orientation in space so that the measured and calculated drift times fit to each other. The relation between drift time and position is taken from GARFIELD simulations. For each orientation of the track with respect to the drift cell in terms of minimum distance to the wire and impact angle to the cell there is a calculated value of the drift time with corresponding error. Furthermore during the track fitting procedure a filtering mechanism is applied which decides whether the found set of wires (cluster or track candidate) from track finding is fake or not and removes wires from the cluster which do not belong to it.

For momentum reconstruction different methods have been developed:

- Method of kick plane
- Spline method
- Runge-Kutta method

The method of kick plane uses tabulated trajectories created using simulated data in order to define the momentum of the particle from the momentum kick. The method of spline uses a cubic spline track model inside the magnetic field for estimation of the track points together with the derivatives at several points inside the field region. The momentum is derived by solving the equation of motion of the charged particle through the field by forcing the particle to travel along the model assumed. The momentum is a parameter of the method which means that there is no need to provide an initial value of the momentum. In the Runge-Kutta Method the equations of motion which are the second order differential equations, are solved by using iterative Runge-Kutta methods taking all initial conditions from spline (momentum) and track fitting (angles and directions).

3.3 Track finder

The information obtained from the MDCs are the hardware addresses of fired wires[2] which are converted into the wire numbers using lookup tables. If one tries to solve the problem by taking all possible combinations of fired wires which might belong to one track, the resulting number of combinations per chamber can be very high. Therefore one needs a filtering mechanism to decrease the number of combinations.

As it was mentioned before, each module is composed of six layers of signal and potential wires under different angles with respect to the bases of the MDC module and seven layers of cathode wires oriented under 90^0 with respect to the bases. The existence of six planes of sense wires with high efficiency allows one to reconstruct track pieces (segments) in each MDC separately. This mode of track finding we will call ”chamber mode” track finding, because information from one chamber is used to obtain a track segment.

[2]The wire which gave a signal above threshold. In the text we will refer to these wires as fired wires.

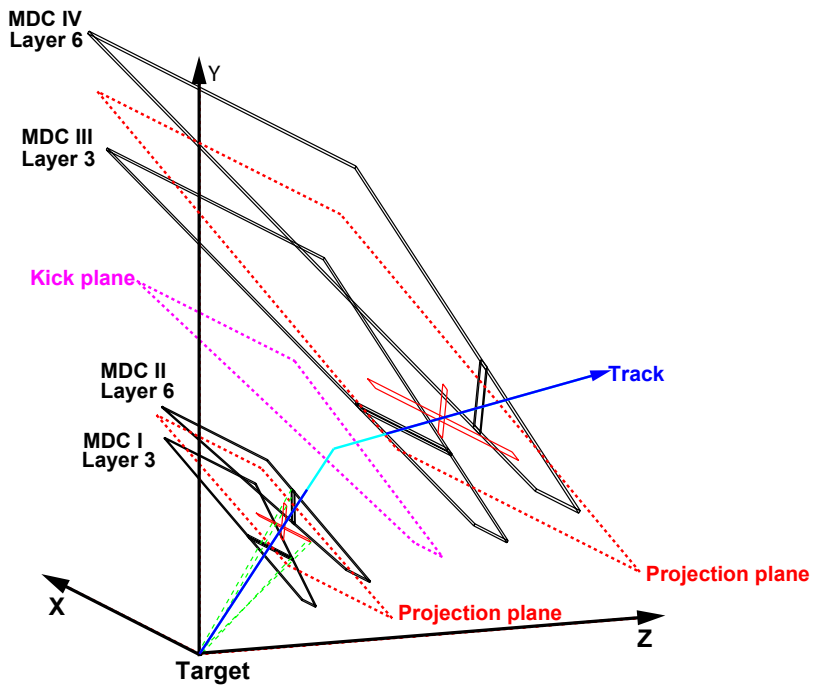

Figure 3.3: Projection of fired wires onto the plane for the combined mode of cluster finding.

The stray magnetic field inside the MDCs was neglected in first approximation, thus allowing to assume a straight track model before and after the magnetic field. Owing to this, it is possible to use information from MDCI-MDCII and MDCIII-MDCIV sets simultaneously, the mode of cluster finder being called a ”combined mode” in this case.

The main idea of the method is to project the images of drift cells corresponding to each wire onto one virtual plane as shown in Figure 3.3 [41, 42, 43]. Due to the extended structure of the target, the projection for each wire is done with respect to the first point (in beam direction) and the last one of the target the net ”shadow” being assumed as a projection of the wire cells on the projection plane (transverse size of the target is neglected). This procedure can be visualized by putting a screen instead of projection plane and illuminating the drift cells of the wire with a linear source of light with the dimensions of the target placed in its position.

The projection plane is selected between MDCI and MDCII so that the transverse sizes

of projected wires from both MDCs onto the plane have approximately the same value[3].

Having projected all fired wires from both MDC's onto the projection plane, one looks for their intersection regions as shown in Figure 3.4. (Wires belonging to the same track coming from the vertex will give an intersection regions on the projection plane). A two dimensional histogram is created[4] and the bins corresponding to the projection of the wire in the projection plane are increased by 1 for each layer [5], so that in the intersection regions we have peaks.

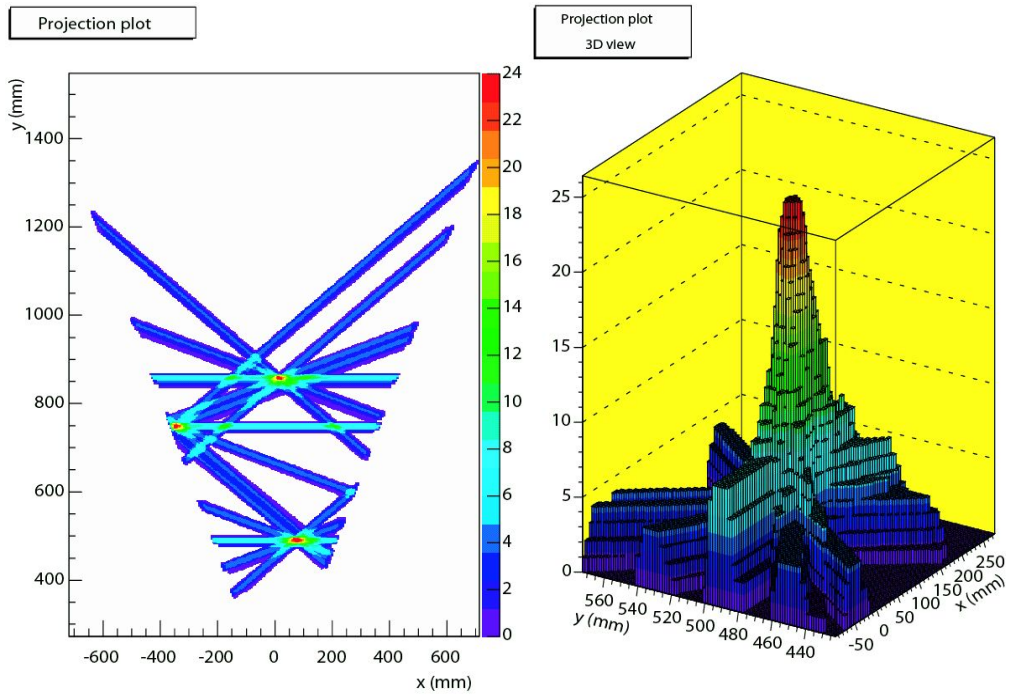

Figure 3.4: Two dimensional (left) and 3 dimensional(right) views of the projected wires

As a peak we consider the set of neighboring bins with a value more or equal to the defined value of H_{min} which is called the level of the cluster finder. The next important step is to set the value for H_{min} to be considered as a candidate for a track. The smaller

[3]Here we describe in general how the track finder works. Depending on the mode of the cluster finding, the projection plane is selected. For example in "chamber mode" the projection plane is selected in the middle of each MDC while in combined and mixed mode it is selected between two corresponding MDC chambers.

[4]The bin size in X direction is 2.7 times bigger than in Y direction due to the better resolution in Y direction coming from the orientations of wires in layers.

[5]If there are two fired wires belonging to the same layer, the bin content is increased by only 1.

the peak level, the more fake track contributions one has. Furthermore the probability of combining of two peaks into one peak is also high in this case. The larger its value, the smaller the efficiency. The optimal choice depends on 3 parameters: occupancy of MDC, efficiency of MDC and minimal number of fired wires for track reconstruction. In our case the minimum number of fired wires for track reconstruction is 4. So in this case it is not reasonable to search peaks of height less than 8 (four from each chamber).

The position of the projection plane being known, it is possible to define the spatial coordinates of the cluster with corresponding errors.

In order to define the position each bin is assigned a weight; $w_i = H_i - H_{min} + 1$. One can now use the standard way of position and resolution finding of the cluster.

$$\begin{aligned} \bar{x} &= \frac{\sum_{i=1}^{n}(x_i W_i)}{\sum_{i=1}^{n} W_i} \\ \bar{y} &= \frac{\sum_{i=1}^{n}(y_i W_i)}{\sum_{i=1}^{n} W_i} \\ \Delta\bar{x} &= \sqrt{\frac{\sum\left(x_i^2 W_i\right)}{\sum W_i} - \bar{x}^2 + \left(\frac{s_x}{2}\right)^2} \\ \Delta\bar{y} &= \sqrt{\frac{\sum\left(y_i^2 W_i\right)}{\sum W_i} - \bar{y}^2 + \left(\frac{s_y}{2}\right)^2} \end{aligned} \tag{3.5}$$

Here s_x and s_y are corresponding bin sizes in x and y direction[6].

After calculation of $\bar{x}$ and $\bar{y}$ of the cluster with the corresponding errors one can calculate the z position of the cluster from the known position of the projection plane; therefore the output information from the track finder are:

- The list of wires with corresponding numbers belonging to the cluster
- The spatial position of the cluster with corresponding errors

The position of the cluster is assumed in first approximation as point on the particle trajectory, the second one being the center of the target.

Sometimes it is necessary to combine different clusters into one. This is done, for example, if there are two close clusters with contributing wires close to each other.

So far we were discussing the method of cluster finding in inner MDCs (before the magnet). The basic idea of cluster finding in the outer MDCs is the same. Nevertheless there are some differences in terms of reference point and the fact that the outer MDCs are parallel to each other.

After reconstruction of the inner segment, its intersection as well as intersection errors with a kick plane (the definition of the kick plane is described in the following sections)

[6]Note that the square of the bin half is added for Δx and Δy because, for example, if only one bin was taken then the errors would be equal to zero.

are calculated. The region in kick plane which is defined as the point of intersection with the errors are taken as a reference point for performing the projection for the outer MDCs. From here on the procedure of cluster finding is similar to that for inner MDCs with kick plane region substituting the target and the projection plane selected between MDC3 and MDC4 being parallel to them. There are some technical differences as well due to the parallel arrangement of the outer MDCs.

One of the important features of the cluster finder is that the rough matching between inner and outer segments is done intrinsically. The outer clusters are looked for within the region on the kick plane defined as the intersection of inner segment with its corresponding errors. This procedure can also be illustrated as an illumination of the outer clusters with the source of light positioned on the intersection point of an inner segment with the kick plane with its dimensions equal to the corresponding errors of the interaction point. This so-called on-fly matching is working quite well if all four MDC chambers are present in the sector. In case of 3 MDC chambers, the matching quality is bad because of the short lever arm and fewer contributing wires. Therefore the number of fake tracks in terms of not matched inner and outer segments is larger as well.

The mode of cluster finder to be used depends on the aim of the analysis, e.g for alignment purposes of the MDC chambers relative to each other the ”chamber mode” should be used. For physics analysis it is preferable to use the ”combined mode” in order to achieve higher resolution. Unfortunately this choice sometimes can be inefficient because of some problems with working layers and layer efficiencies in the setup; therefore in combined mode the requirement of at least 8 wires (4 from each MDC) can decrease the efficiency of the track finder. A third mode for the cluster finder, the ”mixed mode” was developed which projects the wires from both MDCs onto the plane like in combined mode. The condition of at least 4 tracks is put only to the number of wires contributing to found cluster from one MDC chamber. As soon as this condition is fulfilled for any of the chambers there is no such conditions put on the number of wires from another chamber. Nevertheless, in order to increase the resolution obtained, one can put a lower limit on the number of wires from another MDC as well, not necessarily to be 4 as in combined mode, but for example 2.

For the data without magnetic field, it is also foreseen to use for track finding all four MDCs simultaneously. In this case the fired wires from all four MDCs are projected onto one projection plane. This mode of cluster finder was used several times during data taking without magnetic field in order to reconstruct the target position online.

3.4 Track fitter

The information available for track fitting is the number of wires contributing to the cluster with the position of the cluster.

Using this information it is possible to reconstruct a straight line (the second point be-

ing the middle of the target) and calculate the minimum distance between the fired wire and the track with the impact angle to the cell to which there is a corresponding calculated drift time from simulation. In addition the error of the drift cell is also available as a function of minimum distance from the wire and the impact angle which is generated using GARFIELD simulations. Due to the fact that the time offset calculation was based on the fastest particle arrival time, which is set to zero, the measured drift times will be defined with respect to the fastest particle arrival time. Therefore this additional parameter t_{offset} should be added to the calculated drift time (or subtracted from the measured one). During the minimization procedure, this parameter is calculated by forcing the minimization function to be centered at zero. This parameter is not coming only from the fact that the drift time is measured with respect to the fastest particles arrival time. There can be some other reasons which can generate an offset in time, e.g, electronic noise and so on. Therefore we will use a t_{shift} parameter which is equal to t_{offset} plus other components for time shift.

From a mathematical point of view the purpose of the track fitting is to minimize the function [44, 45]:

$$\chi^2 = \sum \frac{(t_i + t_{shift} - T_i)^2}{(\Delta T_i)^2} w_i \tag{3.6}$$

where t_i is the calculated drift time according to the orientation of the reconstructed segment with respect to a given drift cell in terms of distance from the wire and impact angle to the cell, T_i is the measured drift time after time offset subtraction, t_{shift} is the parameter which was described before and w_i are weights

In general the residuals in Equation 3.6 should follow a Gauss distribution if all the wires contributing to the cluster are fired by the track under investigation. These wires we will call ”true” ones, while to the wires contributing from other tracks or the noisy wires in the cluster we will refer to as a ”fake” ones. The contribution of fake wires to the cluster flattens the residual distributions, this in turn makes trouble for traditional least square fitting.

Straightforward application of the maximum likelihood method improves the situation significantly, but this procedure is quite slow and complicated. Therefore we use a weighted least squares fitting [42, 43, 44, 46].

Using the maximum likelihood method for the χ^2 function defined in Equation 3.6 it is easy to show that the obtained weights can be approximated via the functions:

$$w = \begin{cases} \left[1 - \left(\frac{\chi_i^2}{c_4\sigma}\right)^4\right]^2 & |\chi_i| \leq c_w\sigma \\ \left[1 - \left(\frac{\chi_i^2}{c_2\sigma}\right)^2\right]^2 & c_w\sigma \leq |\chi_i| \leq c_2\sigma \\ 0 & |\chi_i| > c_2\sigma \end{cases} \tag{3.7}$$

with $c_w = 2.54$, $c_4 = 3.26$ and c_2=4.19. The second function in 3.7 corresponds to the well known bi-weight of Tukey. The use of the first function is motivated with the fact that

the Tukey bi-weights do not fit the optimal weights obtained from the maximum likelihood method in all regions of the χ^2. The distribution of the weights as a function of χ^2 [7] is shown in Figure 3.5, for a $\sigma = 2.5$ [8].

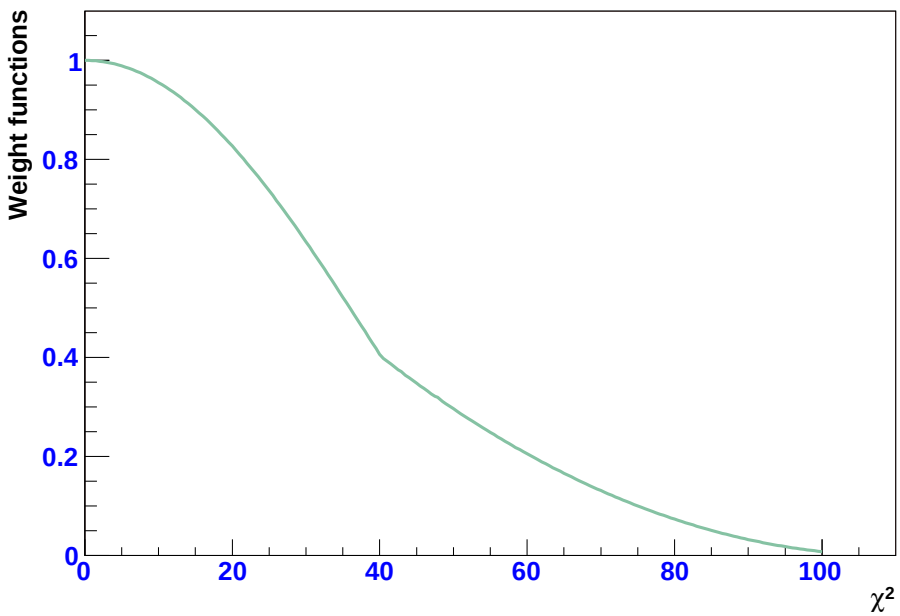

Figure 3.5: The value of the weight as a function of χ^2.

The described weights are used in order to weight each term in Equation 3.6 during the minimization procedure and to filter out the contributing fake wires. In our case we stop filtering if $\sigma < 2.5$.

The first weighting is done without any fit, just by taking the track approximation found by the cluster finder and taking the corresponding calculated times and errors. After assigning a weight in this way the fitting is starting and after each three iterations the new weights are calculated. After filtering out the fake wires from the cluster, the last iteration of fitting is done by setting all weights to 1 for the remaining wires.

We have defined two planes [9] being the first plane of first MDC and the last plane of the second MDC. The intersection points of the reconstructed segments with these planes define the orientation of the track in space[10]; therefore the function χ^2 (See Equation 3.6) depends on four parameters. The offset parameter is calculated each time numerically. We can rewrite Equation 3.6 as:

[7] With $\chi 2$ defined in Equation 3.6.

[8] σ is the width of the weight distribution as shown in Figure 3.5

[9] In "chamber mode", the planes are the first and last planes of each MDC.

[10] As the z positions of the planes are known, one needs only x and y coordinates of the intersection points. Therefore the track is defined with four parameters.

$$\chi^2 = \sum \frac{\left(T_i - f_i\left(x1, y1, x2, y2, t_{shift}\right)\right)^2}{\left(\Delta T_i\right)^2} w_i \tag{3.8}$$

where $x1, y1, x2, y2$ are the intersection points of the track with the corresponding planes, with T_i, t_{shift} and w_i defined in Equation 3.6.

In the minimization procedure the gradient downhill method is used where all the parameters of the function are incremented simultaneously with relative magnitudes so that the resultant direction of travel in parameter space is along the gradient of the minimization function.

The gradient $\nabla\chi^2$ is a vector that points in the direction in which the function χ^2 increases most rapidly and has components in parameter space equal to the rate of change of the function along each axis:

$$\nabla\chi^2 = \sum \frac{\partial\chi^2}{\partial x_k} n_k \tag{3.9}$$

with n_k being a unit vector in the direction of the x_k coordinate axis.

The search starts by changing all parameters simultaneously as:

$$\vec{x}_{k+1} = \vec{x}_k - \frac{\nabla\chi^2}{|\nabla\chi^2|}\Delta R \tag{3.10}$$

where ΔR is an iteration step.

For each changed parameter sets the χ^2 is calculated until after the k-th iteration the function starts to rise. Using χ^2_k, $\nabla\chi^2$ and χ^2_{k+1} it is possible to approximate the function χ^2 with a parabola, whose minimum can be found easily. Finally the minimum is found as:

$$\vec{x}_{k+1} = \vec{x}_k - \frac{\nabla\chi^2}{|\nabla\chi^2|}\Delta R_1 \tag{3.11}$$

Where ΔR_1 is the increment of the parameter corresponding to the minimum of the parabola.

The main disadvantage of this approach is that it needs a lot of iterations. Therefore the following scaling has been used in order to speed up the minimization procedure: the gradient has both magnitude and dimensions and, furthermore usually the components of the gradient do not have the same dimensions, giving for the contour plot of a χ^2 an ellipse. Furthermore, if there is a correlation between parameters, the ellipse is tilted with respect to axis along the given parameters. As an example we can take a function of the form:

$$f = Ax^2 + By^2 \tag{3.12}$$

which depends only on two parameters. The path of the minimization follows the zigzag way as shown in Figure 3.6(a) that is why the method is slow. By making a substitution

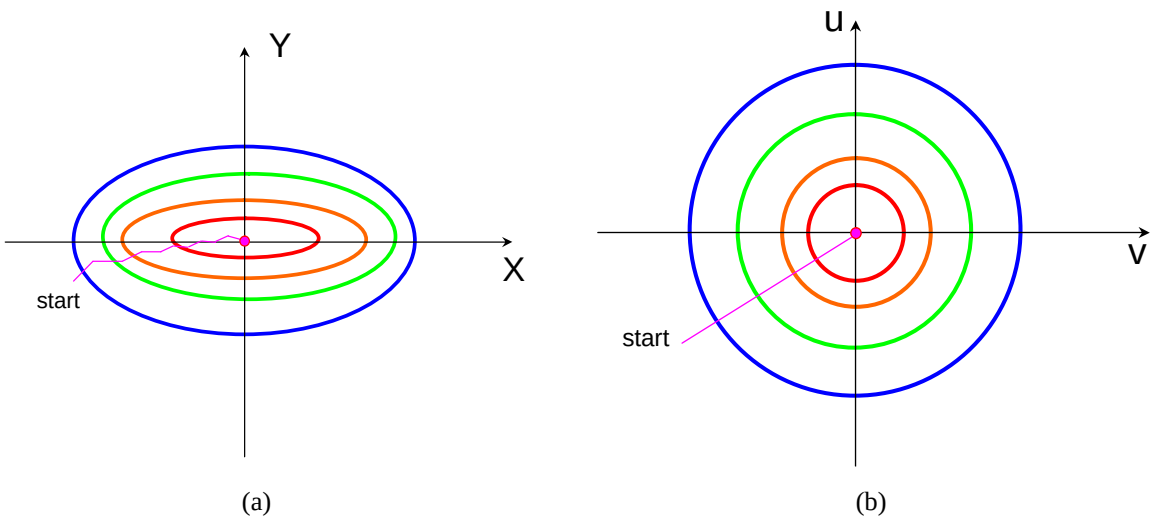

Figure 3.6: Scaling of the fit parameters in order to speed up the minimization procedure.

$$u = x\sqrt{A}$$
$$v = y\sqrt{B} \tag{3.13}$$

one can write write the Equation 3.12 as

$$f = u^2 + v^2 \tag{3.14}$$

which is the equation of a circle. In this case the the gradient is passing through the exact minimum (see Figure 3.6(b)).

The gradient method will not asymptotically approach the minimum because around the minimum the gradient will be equal to 0. A more sophisticated approach is used near the minimum by using the second order partial derivatives:

$$\frac{\partial \chi^2_{k+1}}{\partial x_j} = \frac{\partial \chi^2_k}{\partial x_j} + \sum \frac{\partial^2 \chi^2_k}{\partial x_j \partial x_l} \Delta x_l \tag{3.15}$$

giving a system of linear equations

$$\sum \frac{\partial^2 \chi^2_k}{\partial x_j \partial x_l} \Delta x_l = -\frac{\partial \chi^2_k}{\partial x_j} \tag{3.16}$$

which can be solved against Δx.

The error propagation is done using the standard error propagation procedure.

3.5 Alignment

Both track finder and track fitter need geometrical positions of detectors and detector parts, e.g. chamber position, layer position, wire position, target position and so on. During the mounting process components can be shifted from their ideal positions, and this will affect the precision of reconstruction. The main task of the alignment is to define possible shifts and/or rotations of detector components and to correct for them.

The alignment procedure used in the HADES experiment is based on photometric measurements and cosmic-ray data for the inner chambers, and on straight track reconstruction in runs without magnetic field for the outer ones [47].

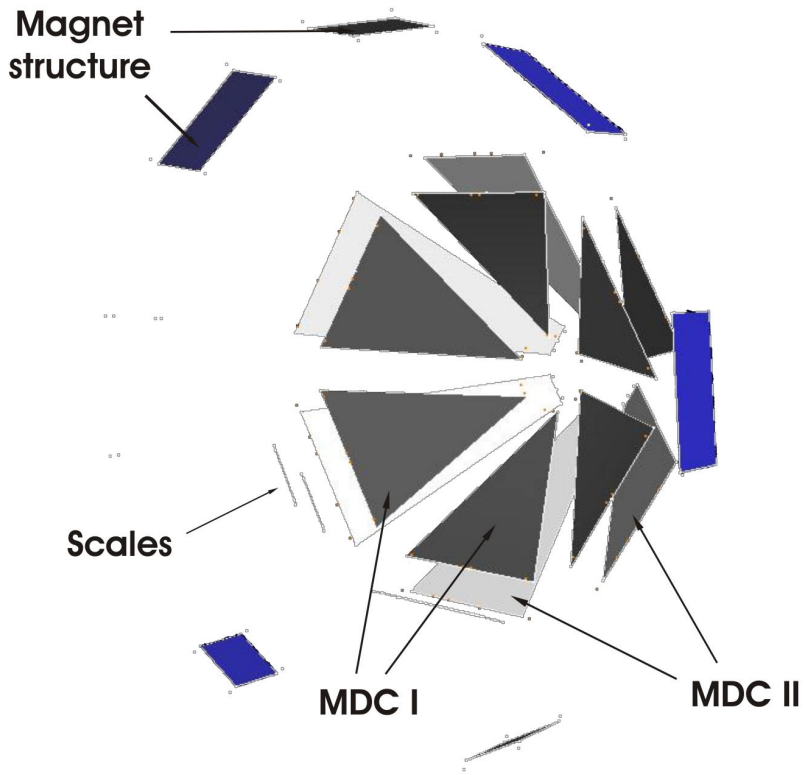

Figure 3.7: 3D view of measured MDCI and MDCII points

Photometry is a photo-camera based method to survey objects in three dimensions. For this purpose 8 Mega pixel mirror reflex camera with a special 20 mm USM wide angle lens was used to take high-resolution pictures of large areas from short distances. The analysis of these pictures was done with the software PhotoModeler 5.0.

First, the camera was calibrated by photographing a special array with fixed positions.

We used special markers which have a typical size of 2-3 cm and were glued directly to the detectors. The software applies a fit to the marker pattern and then calculates the center

of gravity in sub-pixel precision.

First, the photos were taken from MDCII chambers and the magnet support structure and then, after moving the MDCI chambers to measuring position, the same procedure was done for MDC I. After processing in the PhotoModeler software and merging of two projects a 3D-view of the measured points of MDCI,II was obtained as shown in Figure 3.7.

As for the experiment, the MDCI chambers were moved into their nominal positions their relative alignment with respect to MDCII planes was done using cosmic rays which are mainly high-energetic muons at see level [11].

The cosmic rays were taken with an opposite-sector (Tof/Tofino) trigger with a mean data rate of 80Hz.

The track reconstruction method has been optimized for reconstruction of cosmic rays, as they do not come from the target. The reconstruction procedure stays the same with the only difference that as a starting point the META hit is taken.

We start from the point where the position of the MDCI chambers relative to MDCII chambers are fixed by the PhotoModeler survey as described before. Furthermore MDCII chambers are aligned relative to the magnet. From the reconstructed hit and the direction the straight line is constructed and its intersection with the MDCII plane is calculated. The position and inclination of the MDCI chamber is changed until the distance between the reconstructed hit in the MDCII and the intersection point with it reaches a minimum.

The alignment of the outer chambers was done with straight tracks from the target using no-magnetic field data. Since we have an alignment of the inner chambers, as described before, we can use the straight tracks after track reconstruction from these runs to align the outer chambers. MDCI and II are fixed now in position. The positions and inclinations of the outer chambers are varied until the minimum distance between the line, constructed by the reconstructed hits from two inner chambers, and the hits reconstructed in outer chambers reaches its minimum value.

3.6 Matching of hits

The main purpose of the matching algorithm is to find out which of the reconstructed hits from different detector systems corresponds to a given track. As it was mentioned in the previous section, the matching between inner and outer segments is roughly done during track finding.

Here we will discuss the matching procedure of track candidates with the META and RICH detectors. Moreover, the more precise matching between inner and outer segments will be discussed as well.

[11] The relative alignment of the MDCI to MDCII chambers were also done using PhotoModeler software which is assumed as a first approximation for the alignment with comics.

The matching algorithm with the META detectors described here is for the case when there is at least one existing MDC chamber after the magnet in the setup, therefore one has reconstructed outer MDC segments.[12] From the reconstructed outer MDC segment one can construct a straight line in space. At this point we have an information from the META detectors, as well in terms of reconstructed hit (its coordinates), as of module number where the signal was created. Using the module geometry we find the intersection of the line corresponding to the reconstructed outer segment with the module of the META detector.

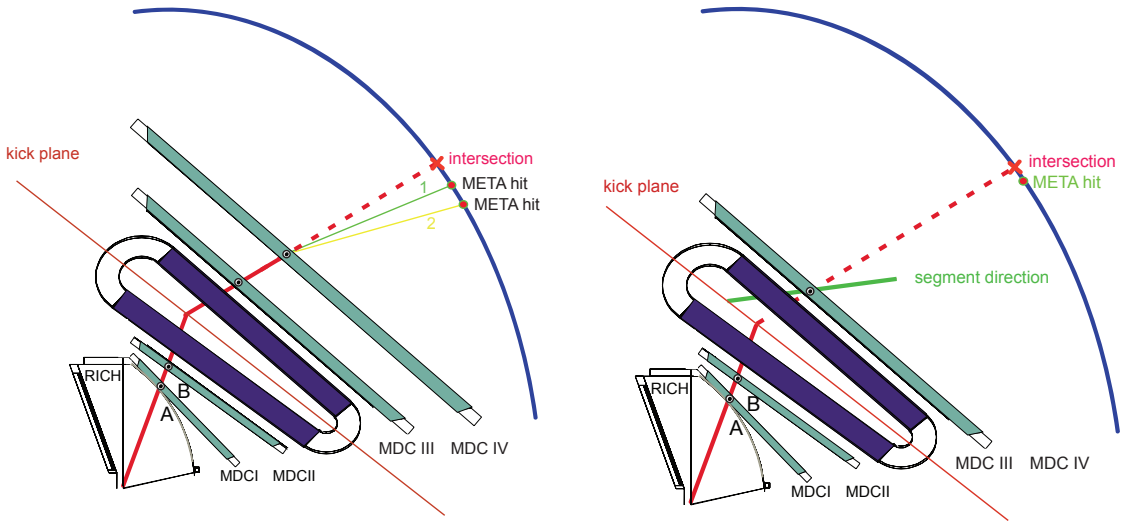

(a) full setup (b) fourth MDC chamber missing

Figure 3.8: Matching of track candidates with META hits in case of (a) four MDC chambers and (b) three MDC chambers.

Having this information we can define quality parameters as:

$$qTof = \sqrt{\left(\frac{xTof - xInt - x_{offset}}{\sigma_x}\right)^2 + \left(\frac{yTof - yInt - y_{offset}}{\sigma_y}\right)^2} \tag{3.17}$$

where $xTof$ and $yTof$ are the coordinates of reconstructed TOF hits, $xInt$ and $yInt$ are the intersection points of the outer MDC segments with the TOF module, σ_x and σ_y are corresponding TOF hit resolutions, while x_{shift} and y_{shift} are introduced so that the residuals in Equation 3.17 are centered at 0.

In a similar way we define the quality parameter for matching with SHOWER hits:

[12]Even in this case different approaches have been used to match the detectors depending whether there are two or one existing MDC chambers after the magnet.

$$qSh = \sqrt{\left(\frac{xSh - xInt - x_{offset}}{\sigma_x}\right)^2 + \left(\frac{ySh - yInt - y_{offset}}{\sigma_y}\right)^2} \tag{3.18}$$

If the value of the quality parameters calculated via Equations 3.17 and 3.18 are smaller than pre-defined values of this parameters (called quality cuts) the object of matching is created [13].

In order to define the quality cut, the distribution of the residuals entering into Equations 3.17 and 3.18 were plotted first and the cuts were applied around the peak of the distributions. In addition to that the shift of the distributions are calculated as well by making the residual distribution to be centered at zero. We have used quite large cut windows in order not to lose statistics at this point.

Each track candidate (matched inner and outer segments) is matched with every META hit in the event satisfying the quality condition described above. The situation is even more complicated because one track candidate can match with several META hits as shown in the Figure 3.8(a).

Therefore there will be some fake combinations which should be removed afterwards. This kind of fake candidates we will call ”meta fakes”. Furthermore there can be the case when one inner segment matches with two outer ones or one outer segment is matched with several inner segments, these fakes being called the ”track fakes”. All these situations can be manipulated with the functions provided in the software (For details see Appendix F).

Matching of the RICH rings with the MDC segments is done by defining two quality parameters:

$$\begin{gathered} qPhi = \frac{(\varphi_{rich} - \varphi_{mdc} - \varphi_{offcet}) * \sin(\theta_{mdc})}{\sigma_{rich}} \\ \Delta\theta = \theta_{rich} - \theta_{mdc} \end{gathered} \tag{3.19}$$

The matching is done if $qPhi$ and $\Delta\theta$ defined in 3.19 satisfy the conditions:

$$\begin{gathered} qPhi < qPhi_{max} \\ \theta_{min} < \Delta\theta < \theta_{max} \end{gathered} \tag{3.20}$$

where the $qPhi_{max}$, θ_{max} and θ_{min} are defined beforehand by plotting the distributions defined in 3.19.

If there are several rings matching with the same inner segment the corresponding ring candidates are stored in an array of defined size (3 in our case), the first one being the best one in terms of quality parameters.

[13] The matching object is also created if none of the META hits are matched with a given track candidate. In this case the value of quality parameters are set to -1.

The matching procedure of the outer segments with the META hits are done in a little different way in case of only one existing outer MDC chamber. In this case the reconstructed angles for outer segments can be wrong. This may happen because of the short lever arm and because of less contributing wires. In this case, during the track fitting, the segment can freely be rotated thus giving the wrong angles at the end. Even if the angular information might not be satisfactory in this case, the hit position which is nothing but the intersection of the segment with the middle plane of the chamber will still be reasonable. Therefore, as one of the reference points we take this hit position. In order to reconstruct the straight line we need another point because we are not using the angular information. This point is taken as the intersection point of the inner segment with the kick plane as shown in Figure 3.8(b). From these two points (point on kick plane and the hit position) we construct a straight line and find its intersection with the META module, the rest of the procedure being analogous to the case of matching with four MDC chambers.

When a particle interacts with the sensitive volume of the TOF detector it can hit several scintillator rods which can be misinterpreted by the TOF hit finder as a series of hits caused by several incident particles and leads in general to overestimation of the event multiplicity. For the set of hits located in the TOF detector the name *TOF cluster* will be used. In order to cluster the hits caused by one particle and to do not cluster the hits caused by multiple particles a special algorithm was created the output of which contains the found clusters with the number of TOF hits entering the cluster (cluster size). On the matching level the candidates are created for TOF cluster and two TOF hits entering the cluster[14]. The situation is more complicated here because the same TOF cluster and/or the hits entering to cluster can match with different track candidates. The conclusion whether the TOF cluster of the hits should be used in the analysis is done with separate algorithm. Currently it was decided to use only cluster information in case of cluster size two and not to use hit information.

Another double counting of META hits can come from a hardware overlap on TOF and SHOWER detectors. In this case, two hits in the META detector will be reconstructed from one track, one of them coming from the TOF detector and another one coming from the SHOWER detector. In this case two matching objects are created, one corresponding to the matching with the TOF hit and another one corresponding to the SHOWER hit. One of these candidates is excluded by an overlap checking algorithm. At the moment the matching only with the TOF hit is taken while matching with the SHOWER hit is excluded because of better resolution of the TOF hit.

On the META matching level broad matching windows are used in order not to lose a tracks on this level. It is foreseen that track cleaning algorithms should be developed in order to remove the fake combinations created on the matching level. This procedure will be discussed in the analysis part of this thesis.

In general there can be several outer segments matching with a given inner segment,

[14]Only the cluster size of two is considered in the matching algorithm.

or several inner segments can match with one outer segment. This matching is done during track finding. In order to remove fake tracks created on this level one can introduce matching qualities of inner segments with outer ones. The quality parameter is introduced as:

$$q = \sqrt{\frac{(X_{in} - X_{out})^2}{\sigma_{Xin}^2 + \sigma_{Xout}^2} + \frac{(Y_{in} - Y_{out})^2}{\sigma_{Yin}^2 + \sigma_{Yout}^2}} \tag{3.21}$$

where X_{in}, Y_{in}, X_{out},Y_{out} are corresponding intersection points of inner and outer segments with the kick plane and σ_{Xin}, σ_{Yin}, σ_{Xout}, σ_{Yout} stand for corresponding errors of the intersection points.

Another alternative would be to calculate the minimum distance between the inner and outer segments, and cut on the distance between that point and the kick plane.

3.7 Kick plane algorithm

As it was already mentioned in previous sections the track segments before and after the the magnetic field can be expressed in a first approximation as straight lines. Because of the toroidal magnetic field in the HADES experiment the tracks are mainly bent in one plane; the inner and outer segments belonging to the same track should meet at some point. In fact, because of the resolution, these segments do not cross exactly, therefore one uses a minimum distance between them in space i.e the vertex defined by these segments. The interesting observation is that if one makes a 3D plot of the coordinates of those vertex points one discovers that they lay in a surface which is called a *kick surface* [48][15].

[15]Sometimes in the text the kick surface is referred to as kick plane.

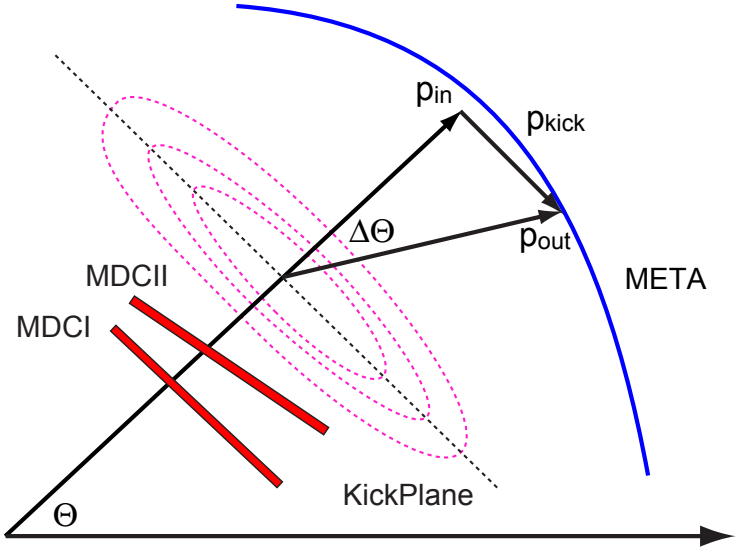

Figure 3.9: Illustration of the kick plane algorithm.

It is clear that a particle with given direction will always hit one spot on the *kick surface* independent of the momentum it has. It can be shown that the momentum of the particle can be calculated using:

$$p = \frac{p_{kick}}{2\sin(\Delta\theta/2)} \tag{3.22}$$

where p_{kick} is the momentum kick and $\Delta\theta$ is the deflection angle as shown in Figure 3.9. p_{kick} depends on the geometry of the field and can be parameterized as function of θ, ϕ and $\Delta\theta$. In order to obtain p_{kick}, simulations were performed where for each point in the kick plane and the deflection angle, the momentum kick was stored in multi dimensional tables (See [48] for details).

This method for momentum determination is used for those sectors where only two MDC chambers existed in the set up; therefore the direction before the magnetic field was provided by MDCI and MDCII, while the direction after the magnetic field was taken from the META hit and the intersection point of the inner segment with the kick plane. The resolution of this method ranges between $7\% - 20\%$ as a function of the momentum of the particle ranging from 100MeV to 1500MeV.

For the sectors where 4 or 3 MDC chambers were mounted the method of spline and Runge Kutta are used to obtain the particle momentum. They are discussed in the next sections.

3.8 Method of spline

A particle's momentum is obtained from its deflection in the magnetic field. In order to define the momentum of the particle by solving a field equations either the trajectory of the particle or the initial momentum should be known with good precision. As there are no detectors in the field region of the HADES spectrometer and the method of kick plane does provide a low precision initial momentum, the model of cubic spline for the trajectory of the particle is assumed.

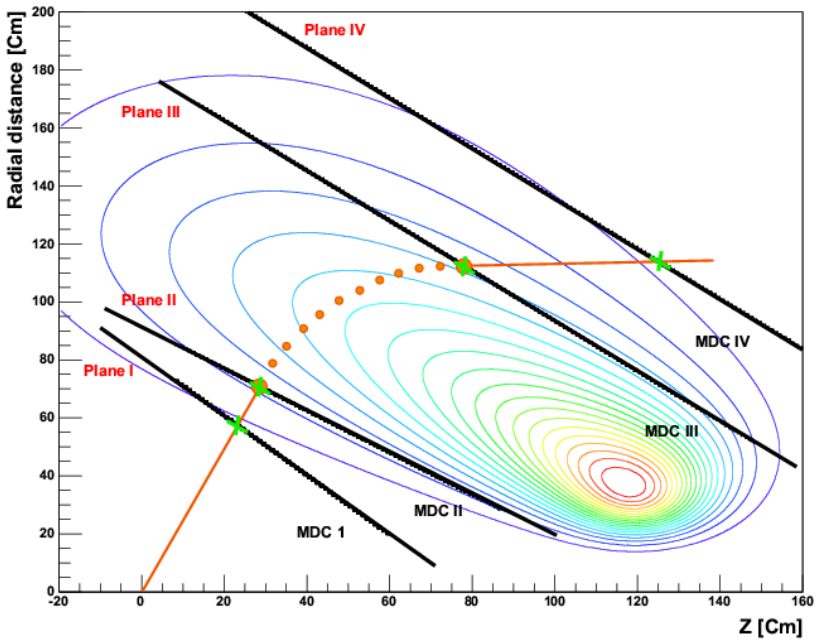

Figure 3.10: Positions of the fixed planes with respect to the main component lines of the magnetic field. The picture is obtained for the middle of the sector, $\phi = 90^0$. The radial distance means $\sqrt{X^2 + Y^2}$. Through intersection points of inner and outer segment with the corresponding planes (green crossings) the spline fit has been performed. The red points are selected from spline curve for which the equations of motion are solved.

3.8.1 Track model assumption

The algorithm described in this section consists of the following steps:

- Assumption of track model inside the magnetic field
- Solution of field equations

In principle we could use any track model which allows an explicit differentiation like a polynomial. If we attempt to represent by an n*th*-degree polynomial a function that is tabulated an n+1 points, we are apt to obtain disappointing results if n is large. The polynomial will necessarily coincide with the data points, but may exhibit large oscillations between points. In addition, if there are many data points, the calculation can become cumbersome. It is often better to make several low-order polynomial fits to separate regions of the function, and this procedure is usually satisfactory for simple interpolation in tables. However, if one wants a smooth function which passes through the data points the result may not be satisfactory [49].

A track model which is, therefore, practically suited is the cubic spline model. We go even one step further and assume a cubic spline method for the field or rather for the track's second derivative. The track model then becomes a quintic spline [50, 51].

A smooth curve that passes through the data points is obtained by requiring the first and second derivatives, as well as the function itself, to be continuous at the data points [52].

The input to the algorithm are reconstructed segments before and after the magnetic field and the field map. We calculate the intersection points of the reconstructed segments with the predefined planes (two before the magnet and the next two behind it) as shown in Figure 3.10. Through the found four intersection points in space we apply cubic spline curves in the YZ and XZ projections. In the next step we select equally distanced points from the obtained curves (X,Y,Z) in the space together with derivatives at those points. We then compute the magnetic field at the selected points using the field map to get three field components B_x,B_y and B_z.

In case of only one outer MDC chamber after the magnet the intersection points of the reconstructed segment from one outer MDC chamber with predefined planes are calculated giving back again four points in the space. However in this case the direction information from reconstructed segment is not used. The direction is calculated using two points the first being the intersection point of the inner segment with the kick plane and the second being the hit position found by tracking. The reason for this is explained in Section 3.6.

3.8.2 Field equations

Charged particle in the magnetic field experiences the Lorentz force which causes it to bend. In the LAB system of the HADES experiment we can write the equation of motion of a particle as:

$$\begin{aligned} \frac{d^2x}{dt^2} &\equiv \ddot{x} = \frac{\dot{y}B_z - \dot{z}B_y}{m} && (a) \\ \frac{d^2y}{dt^2} &\equiv \ddot{y} = \frac{\dot{z}B_x - \dot{x}B_z}{m} && (b) \\ \frac{d^2z}{dt^2} &\equiv \ddot{z} = \frac{\dot{x}B_y - \dot{y}B_x}{m} && (c) \end{aligned} \tag{3.23}$$

As we use a cubic spline approximation for the second derivative on coordinates as well, it is better to write the field equations in terms of second derivatives on coordinates rather than on time. For this we use the expressions[16]

$$\begin{gathered} \frac{\dot{y}}{\dot{z}} = \frac{dy}{dz} \quad and \quad \frac{\dot{x}}{\dot{z}} = \frac{dx}{dz} \\ \frac{d^2y}{dz^2} = \left(\ddot{y}\dot{z} - \ddot{z}\dot{y}\right)/\dot{z}^3 \end{gathered} \tag{3.30}$$

By substituting in 3.30 the expression for $\ddot{y}$ and $\ddot{z}$ from 3.23 we obtain:

$$\frac{d^2y}{dz^2} = \frac{\dot{z}^2 B_x - \dot{x}\dot{z}B_z - \dot{x}\dot{y}B_y + \dot{y}^2 B_x}{\dot{z}^3 m} \tag{3.31}$$

Finally, using the first line of 3.30 together with

$$p = \dot{z}m\sqrt{1 + \left(\frac{dx}{dz}\right)^2 + \left(\frac{dy}{dz}\right)^2} \tag{3.32}$$

we write the field equation in the YZ plane in the following way [17]

[16]By writing

$$\frac{dy}{dt} \equiv \dot{y} = \frac{dy}{dz}\frac{dz}{dt} = \frac{dy}{dz}\dot{z} \tag{3.24}$$

we can obtain

$$\frac{\dot{y}}{\dot{z}} = \frac{dy}{dz} \tag{3.25}$$

and

$$\frac{\dot{x}}{\dot{z}} = \frac{dx}{dz} \tag{3.26}$$

In a similar way using

$$\ddot{y} = \frac{d^2y}{dt^2} = \frac{d}{dt}\left(\frac{dy}{dz}\frac{dz}{dt}\right) = \frac{d^2y}{dz^2}\dot{z}^2 + \frac{dy}{dz}\ddot{z} \tag{3.27}$$

together with

$$\frac{dy}{dz} = \frac{\dot{y}}{\dot{z}} \tag{3.28}$$

we obtain

$$\frac{d^2y}{dz^2} = \frac{1}{\dot{z}^3}\left(\ddot{y}\dot{z} - \ddot{z}\dot{y}\right) \tag{3.29}$$

[17]Note that in order to get the momentum in MeV/c, the right-hand side of the equation should be multiplied by 2.99$[MeV/c]T^{-1}cm^{-1}$.

$$p\frac{d^2y}{dz^2} = k(z)\left(B_x\left(1+\left(\frac{dy}{dz}\right)^2\right) - B_y\frac{dx}{dz}\frac{dy}{dz} - B_z\frac{dx}{dz}\right) \tag{3.33}$$

where $k(z)$ is defined as:

$$k(z) = \sqrt{1+\left(\frac{dx}{dz}\right)^2 + \left(\frac{dy}{dz}\right)^2} \tag{3.34}$$

In an analogous way we can write the field equations in the XZ plane

$$p\frac{d^2x}{dz^2} = k(z)\left(B_x\frac{dy}{dz}\frac{dx}{dz} - B_y\left(1+\left(\frac{dx}{dz}\right)^2\right) + B_z\frac{dy}{dz}\right) \tag{3.35}$$

with $k(z)$ defined in 3.34.

3.8.3 Solution of field equations

Our main goal in this section is to solve the equations 3.33 and 3.35 obtained in the previous section. The right-hand side of these equations can be evaluated at the selected points from the spline fit. Using the spline interpolation on this evaluated expressions we can determine the double integrals. If we denote by A(z) and C(z) the right-hand sides of the corresponding expressions we can evaluate the integrals:

$$\begin{aligned} Y_i &= \int_{u=z_0}^{u=z_i}\left[\int_{v=z_0}^{v=u} A(v)dv\right]du \\ X_i &= \int_{u=z_0}^{u=z_i}\left[\int_{v=z_0}^{v=u} C(v)dv\right]du \end{aligned} \tag{3.36}$$

The right hand sides of 3.33 and 3.34 are the expressions for momentum times the second derivatives. Therefore the obtained solutions will be momentum times the corresponding coordinates. Furthermore we will have two integration constants from double integration. Therefore the solution of the equations 3.33 and 3.35 divided by momentum can be written as

$$\begin{aligned} Yequation_i &= A_1 + A_2(z_i - z_0) + Y_i/P \\ Xequation_i &= B_1 + B_2(z_i - z_0) + X_i/P \end{aligned} \tag{3.37}$$

As we can see from 3.37 the momentum of the particle enters as a parameter to the solutions which can be found by minizing the function

$$(Xspline_i - Xequation_i)^2 + (Yspline_i - Yequation_i)^2 \tag{3.38}$$

where $Xspline_i$ and $Yspline_i$ are the points taken from the first spline fit.

In the HADES experiment, due to the toroidal field, the bending of the particle is happening mainly in one plane which is the new YZ plane after rotation of the coordinate system around the Z axis by an azimuthal angle ϕ of the track. In this new coordinate system the momentum of the particle can be obtained by minimizing the simplified function which leads to 3X3 matrices instead of 5X5 in 3.38.

$$(Yspline_i - Yequation_i)^2 \tag{3.39}$$

The method finds out the momentum of the particle which would move along the assumed track model. This means if the track model is far from the real trajectory of the particle, the found momentum will not be the true one. Most of the deviation from the real trajectory of the particle takes place near the magnetic coils. Therefore the reconstructed momentum differs from the real one as well. For this reason correction parameters have been calculated using simulated data. The correction parameters are created for each bin of the polar and azimuthal angles of the track. In order not to produce the correction parameters for each beam time and new version of the alignment, we introduced fixed planes as discussed at the beginning if this section.

In order to obtain the intrinsic resolution of the method, different simulation files have been generated by shooting single electrons and positrons per event into the spectrometer. The hit points were taken from Geant simulations in order to have pure momentum resolution coming from the method without influence of reconstruction resolution of the hits. In the next step hits were smeared with different resolutions from 60μm to 100μm in Y direction and from 120μm to 200 μm in X direction. The obtained momentum resolution

$$\frac{\frac{1}{p_{Rec}} - \frac{1}{p_{Geant}}}{\frac{1}{p_{Geant}}} \tag{3.40}$$

as a function of the momentum is presented in Figure 3.11(a). For the case where the hit points are taken without any smearing from the Geant simulation the dependance as expected is flat. When one smears the hit points the resolution is much affected for high momenta. This is because the curvature is very small for the high momenta. On the other hand, the curvature is quite high for small momenta and the change of the curvature coming from hit smearing is small compared to it.

The momentum resolution obtained is 0.2% in case of ideal hits. It changes from 0.4% to 1% as a function of momentum ranging from 200MeV to 1500MeV for the hits smeared by 60μm and 120 μm in Y and X directions correspondingly.

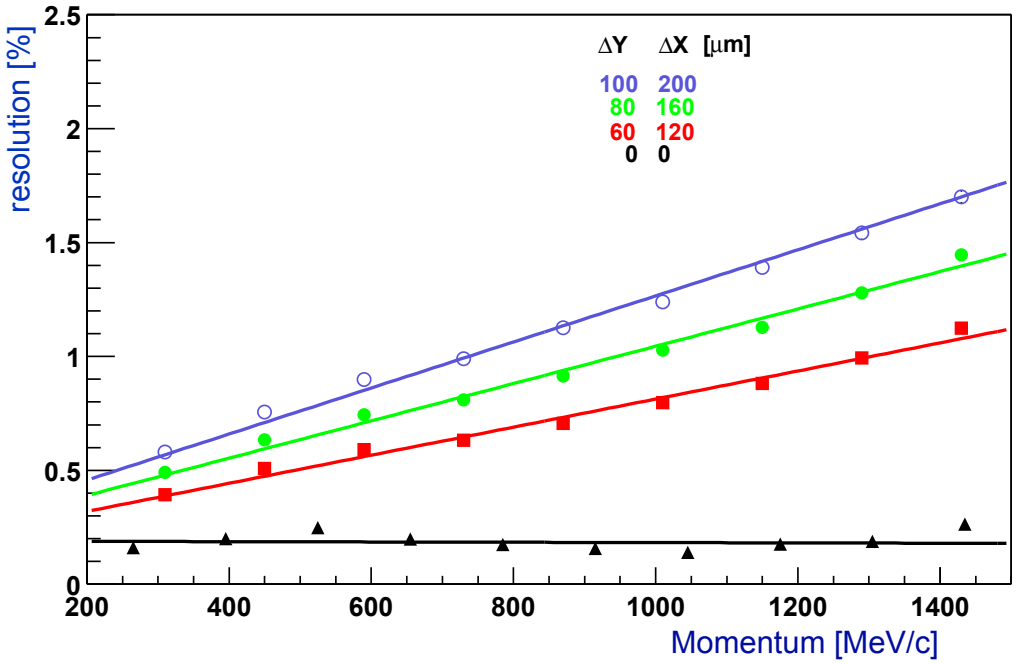

(a) without multiple scattering

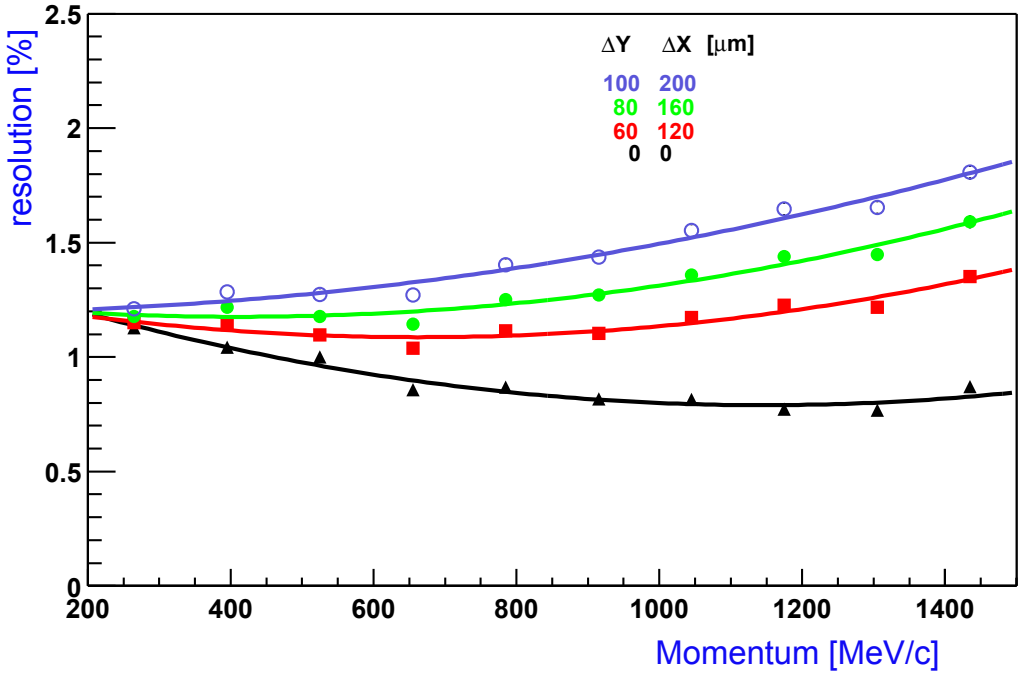

(b) with multiple scattering

Figure 3.11: Momentum resolution as a function of momentum for different resolutions of GEANT hits.

The momentum resolution in case of multiple scattering switched on for different hit resolutions is shown in Figure 3.11(b). As it is seen from the Figure the resolution ranges from 1.2% to 1.4% as the momentum changes from 200MeV to 1500MeV for the hits smeared by 60μm and 120 μm in Y and X directions correspondingly. The reconstruction for the low-momentum part can still be improved if one takes into account the multiple scattering effect in the method.

3.9 Method of Runge Kutta

As was mentioned in section 3.8 for the determination of particle's momentum either the trajectory of the particle or the initial parameters should be known with high precision. In general one needs to solve a second-order field equations for the particle movement in the field. These equations can be solved using fourth order Runge-Kutta method of Nystrom in recursive way, which means each new solution is obtained from the previous one via some relations [53]. In this sense we can speak about a realistic track model along which the particle is moving.

It is clear that for solution of the second order differential equations one needs initial conditions, on the function itself and its first derivatives. All these conditions are provided by the spline method (momentum and polarity) and the track fitter (angles).

From a mathematical point of view the method searches the parameters corresponding to the minimum of the function

$$F = (m - u(\alpha))^T W^{-1} (m - u(\alpha)) \tag{3.41}$$

where m is the measured hits in the MDC chambers, $u(\alpha)$ are the intersection points of the model with the corresponding chambers (with the middle plane where the hit is defined) and α is the matrix of parameters (angles and momentum).

In our case we neglected the correlation between the parameters so the diagonal form of the error matrix was taken.

The minimization procedure is based on least squares fitting, which means solving the linear equations obtained by setting to zero the partial derivatives of the minimization function with respect to the parameters.

Although the Runge-Kutta method is exact one, it is much slower than the spline method.